JAMES | Journal of Advances in Modeling Earth Systems

RESEARCH ARTICLE
10.1029/2024MS004407

Implementation of Dynamic Fire Injection Height in GFDL's Atmospheric Model (AM4.0): Impacts on Aerosol Profiles and Radiation

Arman Pouyaei[1,2], Paul Ginoux[3], Daniel S. Ward[4], Yan Yu[5], and Larry W. Horowitz[3]

[1]Program in Atmospheric and Oceanic Sciences, Princeton University, Princeton, NJ, USA, [2]Cooperative Institute for Modeling the Earth System, Princeton University, Princeton, NJ, USA, [3]NOAA/OAR Geophysical Fluid Dynamics Laboratory, Princeton, NJ, USA, [4]Karen Clark & Company, Boston, MA, USA, [5]Department of Atmospheric and Oceanic Sciences, School of Physics, Peking University, Beijing, China

Key Points:

- Implementation of Sofiev injection scheme for biomass burning (BB) emissions in the AM4.0 model improves aerosol simulation accuracy
- Dynamic injection of BB aerosols reduces net top of the atmosphere clear-sky radiative flux by -0.11 Wm^{-2} and net SFC by -0.38 Wm^{-2}
- Changes in BB injection height influence temperature profile, inducing anomalies in atmospheric circulation

Supporting Information:

Supporting Information may be found in the online version of this article.

Correspondence to:

A. Pouyaei,
apouyaei@princeton.edu

Citation:

Pouyaei, A., Ginoux, P., Ward, D. S., Yu, Y., & Horowitz, L. W. (2025). Implementation of dynamic fire injection height in GFDL's Atmospheric Model (AM4.0): Impacts on aerosol profiles and radiation. *Journal of Advances in Modeling Earth Systems*, *17*, e2024MS004407. https://doi.org/10.1029/2024MS004407

Received 19 APR 2024
Accepted 23 FEB 2025

Author Contributions:

Conceptualization: Arman Pouyaei, Paul Ginoux
Data curation: Arman Pouyaei, Yan Yu
Formal analysis: Arman Pouyaei, Paul Ginoux
Methodology: Arman Pouyaei, Paul Ginoux
Software: Arman Pouyaei, Daniel S. Ward, Larry W. Horowitz
Supervision: Paul Ginoux
Validation: Arman Pouyaei
Visualization: Arman Pouyaei

Abstract Wildfires inject aerosols into the atmosphere at varying altitudes, modifying long-range transport, which impacts Earth's climate system and air quality. Most global climate models use prescribed fixed-height injections, not accounting for the dynamic variability of wildfires. In this study, we enhance the injection method of biomass burning aerosols implemented in the Geophysical Fluid Dynamic Laboratory's Atmospheric Model version 4.0, shifting to a more mechanistic approach. We test several injection height schemes to assess their impact on the Earth's radiation budget by performing 18-year global simulations. Comparison of modeled injection height from the mechanistic scheme with observations indicates error within instrumental uncertainty (less than 500 m). Aerosol Optical Depth is systematically underestimated due to biases in the emission data set, but the mechanistic scheme significantly reduces this bias by up to 0.5 optical depth units during extreme wildfire seasons over boreal forests. In term of the vertical profile of the aerosol extinction coefficient, a comparison with satellite observations indicates significant improvement below 4 km altitude. Dynamic injection of biomass burning emissions changed the net clear-sky radiative flux at top of the atmosphere regionally (± 1.5 Wm^{-2}) and reduced it by -0.38 Wm^{-2} at the surface globally, relative to a baseline with no fire emissions. The temperature gradient anomaly associated with the dynamic injection of absorbing aerosols affects the atmospheric stability and circulation patterns. This study highlights the need to implement dynamic injection of fire emissions to simulate more accurately the atmospheric distribution of aerosols and their interactions with Earth's climate system.

Plain Language Summary Wildfires influence climate by emitting aerosols into the Earth's atmosphere. These aerosols reflect and absorb sunlight, which perturbs the Earth's radiation budget. The present work involves the replacement of fixed-height injection of aerosols from wildfires by a mechanistic scheme, which depends on atmospheric stability and fire radiative power. We included this new injection scheme into GFDL's AM4.0 model to account for spatial and temporal variability of wildfire intensities. This allowed us to simulate the aerosol distribution more consistently. The comparison of our model's results with satellite data indicates satisfactory results with marginal error of less than 500 m. The major effects of this scheme are to change the aerosol extinction profiles, which affects radiative fluxes by ± 1.5 Wm^{-2} regionally at top of the atmosphere and by -0.38 Wm^{-2} globally at surface. These atmospheric perturbations change temperature profiles which induce anomalies in atmospheric circulation.

1. Introduction

Wildfires affect the Earth's climate systems through complex mechanisms starting with the aerosol emission into the atmosphere. These past few years have witnessed a surge in wildfire intensity and frequency in some regions, largely attributed to global warming and anthropogenic activities (Ford et al., 2018; IPCC, 2022; Westerling et al., 2006; Yu et al., 2021). Aerosols emitted by fires affect climate by altering absorption and scattering of solar radiation (Veira, Kloster, Schutgens, & Kaiser, 2015), atmospheric stability (Dowdy & Pepler, 2018), circulation patterns (Tosca et al., 2013; Yasunari et al., 2021), and precipitation dynamics (Jiang et al., 2020). These BB aerosols may feed back on fire emissions through climate adjustments, impacting photosynthetic efficiency (Malavelle et al., 2019). Fire aerosols also provide important sources of soluble iron that fertilize the ocean (Mahowald et al., 2017) and Light Absorbing Particles that decrease snow albedo (Flanner et al., 2007, 2009). In addition, gaseous compounds emitted by fires influence tropospheric ozone levels and may substantially affect

Writing – original draft: Arman Pouyaei
Writing – review & editing: Paul Ginoux, Daniel S. Ward, Yan Yu, Larry W. Horowitz

the atmosphere's oxidizing capacity (Jaffe & Wigder, 2012; Xu et al., 2021). Therefore, understanding the complex interactions of fire-emitted aerosols and trace gases within the Earth's components (atmosphere, ocean, and cryosphere) is a significant factor to properly simulate the coupled climate-carbon cycle with Global Circulation Models (GCMs).

One of the factors affecting wildfire-climate interactions in GCMs is smoke plume injection height. During a wildfire, plumes of aerosols arise by buoyancy flux induced by the convective heat generated by fire itself (Paugam et al., 2016). Once the updraft stabilizes, it detrains aerosols at a certain altitude in the atmosphere, which is referred to as the smoke plume injection height or injection height. There have been several attempts to calculate fire injection heights in chemical transport models and GCMs (Paugam et al., 2016). Methods of simulating injection are either empirical (Briggs, 1984), deterministic (Freitas et al., 2007; Rio et al., 2010; Sofiev et al., 2012), or statistical (Val Martin et al., 2012). A deterministic approach with dynamic variability is more desirable in coupled climate models since the information from a fire model can be coupled to the atmosphere to understand the land-atmosphere interactions. The significant variability and sensitivity of fire emissions strongly influences smoke plume behaviors, affecting their duration, chemical transformations, and ultimately the radiative budget (Lu et al., 2024). Initially, Briggs (1984) developed a simple parametrization linking smoke plume height to buoyancy flux using experimental data. Advancing further, Freitas et al. (2007) created a detailed plume rise model that solves vertical momentum, thermodynamics, and water phase continuity equations, but its buoyancy heat flux calculations from fires make it computationally demanding. On the other hand, Sofiev et al. (2012) developed a semi-empirical deterministic approach for plume dynamics that is physics-based and computationally efficient, using a unique equation based on Fire Radiative Power (FRP) and atmospheric stability to determine plume injection height. This method, ideal for large-scale climate models due to its lower computational needs, relies heavily on high-quality input data for accurate results.

The need to move from a fixed injection height method (Dentener et al., 2006) to a dynamic and deterministic injection scheme has been discussed in literature. For example, an integration of Sofiev's parameterization into atmospheric general circulation model revealed that $5.2 \pm 1.0\%$ of BB aerosols reach the free troposphere with a radiative forcing (RF) of -0.20 ± 0.07 Wm^{-2} (Veira, Kloster, Schutgens, & Kaiser, 2015). Similarly, Rémy et al. (2017) used daily fire injection data from the Global Fire Assimilation System in the Composition Integrated Forecasting System, enhancing the accuracy of aerosol extinction profiles. Furthermore, deterministic schemes, when applied in regional community chemical transport models, showed promising results in predicting fire plume timing and location (Li et al., 2023; Pouyaei et al., 2023; Ye et al., 2021). Menut et al. (2021, 2018) implemented a modified version of the Sofiev scheme into a chemistry-transport model focusing on Central African BB emissions and showing distinct pollutant pathways depending on emission altitude. Moreover, Zhu et al. (2018) implemented the monthly gridded injection heights provided by statistical analysis of Multi-angle Imaging SpectroRadiometer (MISR) plume heights (Martin et al., 2018) into the GEOS-Chem model and showed improvements in simulation of monthly mean surface carbon monoxide during periods of large wildfires. Different injection schemes can variably impact surface concentrations of particulate matter, and therefore the exceedance level of air quality standards, affecting early warning of extreme air pollution episodes at local levels during large wildfire events (Li et al., 2023). In a recent work, Lu et al. (2024) incorporated the Freitas plume-rise model into the DOE's Energy Exascale Earth System Model Version 1 (E3SMv1) and found a larger carbonaceous aerosol burden, leading to 0.13 W m^{-2} warming at the TOA compared to the default E3SMv1 injection method. These findings highlight the essential role of plume height parametrization in enhancing the accuracy and effectiveness of both regional and global climate models.

Building on the importance of accurate plume height parametrization, it's crucial to address the uncertainties within these schemes as significant underestimation of simulated plume height is observed in the earlier empirical schemes compared to MISR measurements (Raffuse et al., 2012). For example, the Sofiev scheme's exclusion of factors like fire size, wind drag, and entrainment influences plume heights estimations (Freitas et al., 2007, 2010; Rio et al., 2010). Additionally, Val Martin et al. (2012) highlighted the Freitas scheme's low sensitivity to fire area and heat flux, suggesting that a simplified relationship between FRP and atmospheric stability could be effective for plume height parametrization in wildfire scenarios. Besides, its requirement for calculating injection height for each fire through numerical integration of a system of equations renders this approach computationally intensive (Guan et al., 2008). Furthermore, the Freitas scheme can overestimate fire radiative flux by up to 25 times, especially in forest fires, leading to an overestimation of wildfire smoke injection into the free troposphere (Thapa

et al., 2022). Despite these uncertainties associated with injection schemes, they offer significant advantages over fixed injection height models.

Implementing a mechanistic plume injection scheme is crucial for advancing efforts toward interactive modeling of wildfires aerosol in the Earth's climate system (Fasullo et al., 2023; Lawrence et al., 2019) and improving air quality forecasting (Li et al., 2023). This integration, which includes fire emission calculations and injection heights, stems from the growing interest on understanding of chemistry-climate interactions and their impact on future climate projections (Levy, Horowitz, et al., 2013; Rabin et al., 2017; Ramanathan et al., 1987). The Geophysical Fluid Dynamics Laboratory's (GFDL) AM4.0/LM4.0 model (Zhao et al., 2018a), which is included in the GFDL Coupled Model CM4 (Held et al., 2019), participated in the sixth Coupled Model Intercomparison Project (Eyring et al., 2016). It uses fixed injection heights for fire emissions from trace gases and carbonaceous aerosols (Dentener et al., 2006), and a simple planetary boundary layer (PBL) injection for BB SO_2 emissions. Our overall modeling objective is to first replace the existing static injection scheme by a computationally efficient mechanistic scheme, which will be followed by its implementation into the dynamic fire model of GFDL's Land Model version 4 (LM4) (Ward et al., 2018; Xie et al., 2022).

To this end, we implemented the mechanistic Sofiev injection scheme along with surface injection, and fixed height injection into GFDL's AM4.0 model and ran an 18-year simulation (2003–2020) to understand the impact of wildfire injection height on vertical profiles of aerosol concentrations and direct radiative effects. We discuss the methods and data used in the study in Section 2. Section 3 provides a description on the experimental design setup. In Sections 4 and 5, we compare the vertical distribution and optical properties of aerosols with satellite retrievals and in-situ observations. In Section 6, we analyze the impact of the injection scheme on the global distribution of extinction profiles and aerosol layer height. Section 7 analyzes the impact of dynamic injection on the radiation budget and Section 8 examines its climate response. Our research aims to significantly enhance the understanding of BB aerosol injection in climate models, contributing to more accurate climate projections.

2. Methods and Data

In this section, we discuss the model that we used as the basis for our analysis. Next, we provide general description of observation data sets used for model evaluation and for experimental design. Then we discuss the Sofiev plume injection scheme which was selected to simulate mechanistic integration of plume heights.

2.1. AM4.0 Model Description

GFDL's AM4.0 is the fourth-generation global atmospheric model, developed as part of the GFDL efforts toward coupled Earth system modeling. The AM4.0 model was developed based on the previous-generation AM3.0 and HiRAM models (Donner et al., 2011; Zhao et al., 2009). Its dynamical core is a hydrostatic version of GFDL's Finite-Volume Cubed-Sphere Dynamical Core (FV3) (Harris & Lin, 2013). The horizontal grid uses cubed-sphere topology of 6 faces with 96 × 96 grid boxes per cube face (approximately 100 km grid size). The number of vertical levels is set at 33, with relatively crude resolution of the stratosphere with model top at 1 hPa (Zhao et al., 2018b). The model results are saved either daily (aerosol properties) or monthly (climate properties).

The model has a bulk aerosol representation, including black carbon (BC), organic carbon (OC), sulfate, mineral dust, and sea salt. The size distribution of BC, OC, and sulfate aerosol types are prescribed as lognormal, however, for dust and sea salt it is discretized into five bins from 0.1 to 10 μm radius. The concentrations of aerosols (including BB aerosols) are calculated based on their emissions (and precursor emissions), chemical production for sulfate and secondary organic aerosols (SOA), dry and wet depositions, transport by advection, and dry and wet convection. Black carbon and primary OC are converted from hydrophobic to hydrophilic state with an e-folding time of 1.44 days. Chemical production of sulfate is calculated using a monthly mean 20-year climatology of oxidants simulated by AM3 (Naik et al., 2013), which was done using the MOZART comprehensive mechanism of ozone chemistry (Horowitz et al., 2003). Natural terrestrial SOA are formed directly from biogenic terpene emissions, with a variable yield factor ranging from 0.11 per molecule at latitudes below 20° to 0.55 at the poles (Donner et al., 2011). Oceanic SOA is produced based on the organic sea-spray source function described by O'Dowd et al. (2008). Anthropogenic SOA, meanwhile, is generated from the oxidation of 10% of climatological butane by hydroxyl radicals (Donner et al., 2011). Detailed description of the cloud microphysics and convection scheme can be found in Guo et al. (2021, 2022) and Zhao et al. (2018b). To avoid the need for long

spin-ups to equilibrate the vegetation state, we assume static vegetation for present climate as simulated by the AM4.0 historical run from CMIP6.

The model simulations for BB aerosol injection experiments are performed following the Atmospheric Model Intercomparison Project (AMIP) experimental protocols (Gates, 1992) for years 2003–2020, using updated daily BB emissions for BC, OC and sulfur dioxide (SO_2) from Global Fire Emissions Database (GFED) version 4.1s (Randerson et al., 2015), with horizontal wind components nudged to the National Centers for Environmental Prediction (NCEP) global reanalysis data set (NCEP/NCAR Global Reanalysis Products, 1948-continuing [Dataset], 2024) using a relaxation method, with the relaxation timescale being 6 hr (Li et al., 2008). This particular model setup has been designed to allow consistent evaluation with observations on synoptic time scales. We also performed experiments without any nudging to study the fast climate response. The period 2003–2020 was selected to encompass a range of varying BB activities (e.g., associated with different ENSO phases), and to align with the availability of key observational data sets. In AMIP mode, the model is driven by time-varying boundary conditions, and natural and anthropogenic forcings developed in support of CMIP-6 (Eyring et al., 2016), extended for 2015-onward by SSP2-4.5 scenario. Observed gridded sea surface temperature and sea-ice concentration boundary conditions following the reconstruction methodology of Taylor et al. (2000). For radiation calculations, global monthly mean concentrations of greenhouse gases (GHGs) are specified from Meinshausen et al. (2017). The shortwave and longwave radiation algorithms are described by Zhao et al. (2018b). Here, briefly, aerosols interact with radiation through three optical properties: the extinction coefficient, the single scattering albedo, and the asymmetry parameter. These parameters are precalculated using a Mie code at multiple wavelengths from Lyman-alpha to microwave. For hygroscopic particles, the size variation with relative humidity is precalculated from the deliquescence point to 97% relative humidity. In addition, we assume internal mixing of sulfate with BC by considering a volume-weighted average of their refractive indices. The values of optical depth and single scattering albedo are extracted at different wavelengths in the visible for comparison with observations (e.g., 440 nm for AERONET, 550 nm for Cloud-Aerosol Lidar with Orthogonal Polarization (CALIOP) and MODIS).

In the original AM4.0 configuration of Zhao et al. (2018a), BB aerosol injection is treated inconsistently between aerosols. The BB emissions of carbonaceous aerosols (BC and OC) were injected following the AeroCom III project recommendations to distribute emission into 6 different altitude bands depending on wildland fire location and type (Dentener et al., 2006). According to AeroCom III recommendations, fire emissions were continuously injected: below 1 km altitude for tropical regions, below 2 km altitude for temperate regions, 40% in 2–3 km altitude while 60% below 2 km altitude for Boreal Eurasia region, and 40% in 3–6 km altitude while 60% below 3 km altitude for Boreal Canada (see Table 4 in Dentener et al., 2006). Instead of using the same vertical distribution of emission for all aerosols emitted by BB, SO_2 was uniformly distributed throughout the diagnosed PBL. This static representation of aerosol injection missed the variability associated with wildfires and atmospheric conditions. The vertical profile of BB aerosol emissions is crucial as it directly influences aerosol transport and atmospheric lifetime, their function as cloud condensation nuclei and ice-nucleating particles (altering global cloud patterns), and, consequently, impacts RF calculations.

2.2. MODIS Aerosol Optical Depth and Fire Radiative Power

We used MODIS Terra level-3 gridded Collection 6.1 aerosol products, in particular the quality-assured merged land and ocean Aerosol Optical Depth (AOD) at 550 nm (Sayer et al., 2014) for validating modeled AOD. The estimated uncertainty of retrieved AOD depends on the retrieval algorithm. For the Dark Target algorithm, Levy, Mattoo, et al. (2013) provide an uncertainty of 0.05 ± 0.15*AOD, and for the Deep Blue algorithm, Sayer et al. (2014) give an estimated error of 0.09 ± 0.56*AOD. Moreover, we used fire intensity information from the MODIS sensor onboard NASA Terra/Aqua for input to our dynamic injection scheme. As a proxy for fire intensity, we extracted the FRP values from the Fire Information for Resource Management Systems (FIRMS), which provides daily global active fire product from Terra (10:30 a.m. local overpass time) and Aqua (1:30 p.m. local overpass time) satellites (MODIS/Terra Thermal Anomalies/Fire Daily L3 Global 1 km SIN Grid V061 [Data set]). The global active fire product is calculated based on MODIS Thermal Anomalies and Fire Daily Version 6.1 data at 1 km spatial resolution (Giglio et al., 2016).

We resampled the FRP values on a 1.0 by 1.25° resolution grid, which is close to AM4.0's resolution, as input for the plume height calculations. To keep track of the variability of FRP between 1-km MODIS data and the much

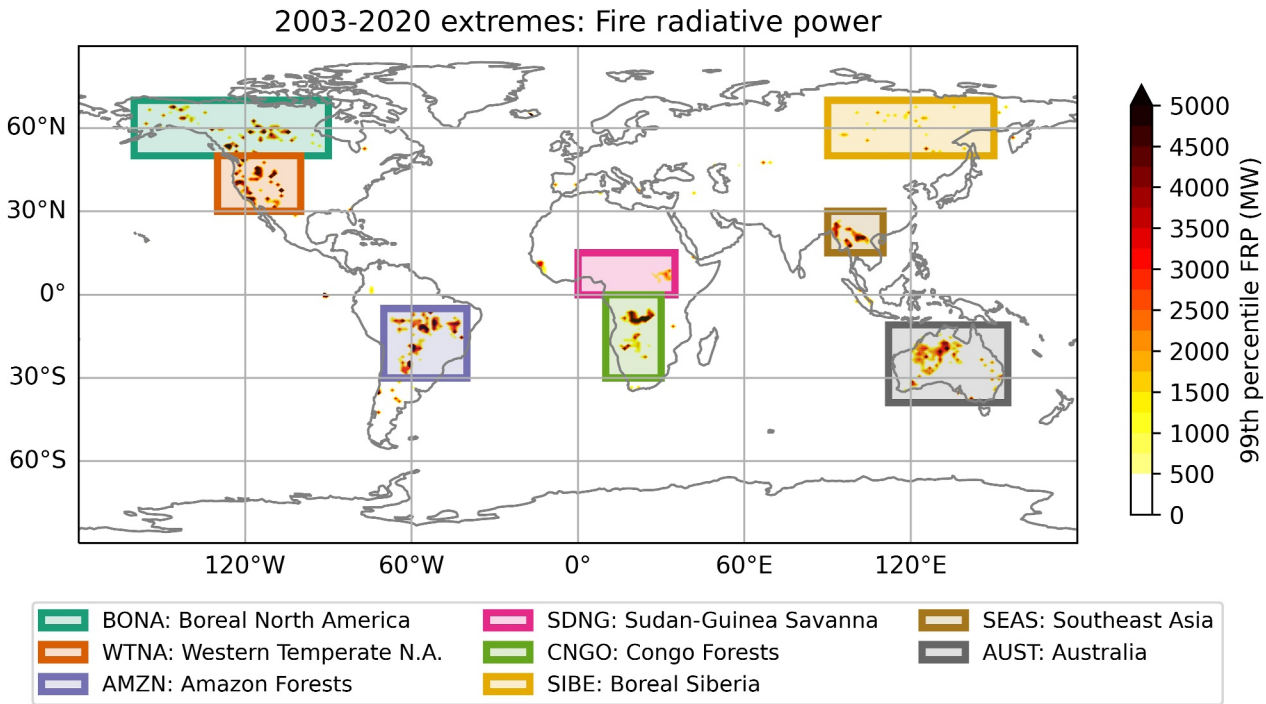

Figure 1. 99th percentile MODIS fire radiative power values for extreme wildfires and the regions where the extreme wildfires mostly happen.

coarser model grid, we calculated different percentiles of FRP values (10th, 25th, 50th, 75th, 90th, and 99th percentile) within each model grid. To analyze the most prominent impacts from BB emission injections we defined regions with sustained extreme wildfires with at least five continuous days of 99th percentile of FRP values above 500 Megawatts. Through visual inspection we selected eight different regions with sustained extreme wildfires (Figure 1). Our analysis of the FRP percentiles for all BB regions (Figure S1 in Supporting Information S1) show that North America, Australia, and Congo have higher FRP values for the 75th, 90th, and 99th percentiles than other regions.

2.3. AERONET Aerosol Optical Depth

To account for the temporal changes in optical properties caused by BB aerosols and extract the most dominant changes from aerosol injection in various wildfire seasons, we used quality-assured daily extinction coefficient level 2 retrievals at 440 nm from the Aerosol Robotic Network (AERONET) version 3 database for the period of 2003–2020 (Sinyuk et al., 2020). The AERONET global network provides direct Sun measurements via radiometers every 15 min at various nominal wavelengths. The estimated uncertainty in AOD measurements is primarily due to calibration uncertainty ranging ~0.010 to 0.021 for field instruments (Giles et al., 2019). AERONET data, with its high temporal resolution in AOD measurements, complements MODIS data for validating our model simulations.

2.4. CALIPSO Extinction Coefficient

To directly evaluate the vertical distribution of aerosol injection, we compare our simulated extinction profile at 550 nm with quality-screened cloud-free gridded monthly extinction profile at 532 nm derived from the Cloud-Aerosol Lidar and Infrared Pathfinder Satellite Observation (CALIPSO) measurements retrieved by the CALIOP instrument (Tackett et al., 2018). All level 3 parameters are derived from the version 4–20 level 2 of this data set which is available from June 2006 until July 2020 (CALIPSO Lidar Level 3 Tropospheric Aerosol Profiles, Cloud Free Data, Standard V4-20 [Data set]).

2.5. MISR Plume Height Project

The Multi-angle Imaging SpectroRadiometer (MISR) instrument on the NASA Terra satellite provides a unique opportunity for acquiring global multiangle imagery especially focused on wildfire smoke plumes. By using an interactive visualization code called MISR INteractive eXploer (MINX), users can extract wildfire plume heights. The MISR Plume Height Project is a publicly available database of wildfire smoke plume heights generated by MINX software (MISR, 2023). This database has plume height and other fire related information from wildfires during 2008–2011 and summers of 2017 and 2018, in addition to other plumes which have been provided since. The database has been widely used to validate plume rise models and study the dynamics of fires (e.g., Raffuse et al., 2012; Sofiev et al., 2012; Val Martin et al., 2012). We extracted the plume height data and used the maximum plume heights in our study (MISR, 2023). Although MISR's local passing time is around 10:30 a.m. before the early afternoon peak intensity of wildfires (Val Martin et al., 2010), it serves as a vital and reliable validation tool, allowing us to benchmark the accuracy of injection height predictions against observed data.

2.6. Sofiev Injection Height Scheme

For this research, we use the Sofiev et al. (2012) scheme to parametrize plume injection height in AM4.0. The Sofiev scheme predicts wildfire plume heights using three input variables: PBL height, FRP, and Brunt-Väisälä frequency in the free troposphere. By calibrating parameters with MISR plume height project data set, they introduced the following generic formula:

$$H_{\mathrm{p}} = \alpha H_{\mathrm{pbl}} + \beta\left(\frac{\mathrm{FRP}}{P_{\mathrm{f0}}}\right)^{\gamma} \exp\left(-\delta N_{\mathrm{FT}}^2 / N_0^2\right) \tag{1}$$

α is the part of the PBL which passes into plume height calculation, β constraints the share of the contribution of the fire intensity, P_{f0} is constant reference fire power (10^6 W), γ determines the power-law dependence on FRP, δ defines the dependency on stability in free troposphere (which is represented by the squared Brunt-Väisälä frequency, N_{FT}^2), and N_0^2 is the reference value for squared Brunt-Väisälä frequency (2.5×10^{-4} s^{-2}). The calibration gave the following parameters:

$$\alpha = 0.24, \quad \beta = 170 \text{ m}, \quad \gamma = 0.35, \quad \delta = 0.6 \tag{2}$$

In addition, Sofiev et al. (2012) introduced a two-step mechanism for parameters in an attempt to reduce biases from plume height predictions compared to MISR plume heights. The first step uses the parameter values given in 2. In the second step, the height is recalculated based on the following parameters, depending on if the result from first equations is above or below PBL height:

For PBL plumes:

$$\alpha = 0.15, \quad \beta = 102 \text{ m}, \quad \gamma = 0.49, \quad \delta = 0.0 \tag{3}$$

And for FT plumes:

$$\alpha = 0.93, \quad \beta = 298 \text{ m}, \quad \gamma = 0.13, \quad \delta = 0.7 \tag{4}$$

Following the works from Veira, Kloster, Wilkenskjeld, and Remy (2015) and Menut et al. (2021), we also experimented with an empirical correction of FRP from MODIS data in the case of strong fires (Peterson et al., 2013, 2014) by scaling the calculated plume Hp with an ad hoc H_{deep} altitude:

$$\mathrm{FRP}_{\mathrm{corrected}} = \mathrm{FRP} \times \left(\frac{H_p}{H_{\mathrm{deep}}}\right)^{\varepsilon} \tag{5}$$

$$H_{\mathrm{deep}} = 1500 \text{ m}, \quad \varepsilon = 0.5 \tag{6}$$

This method checks if the calculated plume (H_p) is higher than H_{deep}; if so, it recalculates the plume height with the corrected FRP via Equation 2. In our implementation, H_{pbl} and N_{FT}^2 are calculated online within the AM4.0

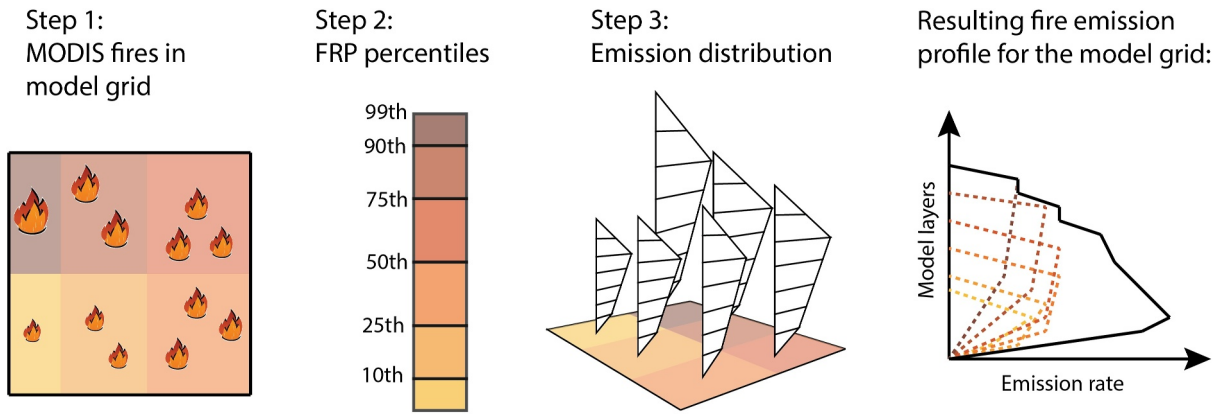

Figure 2. Scale-aware emission distribution; step 1: extract all the MODIS fires in model grid, step 2: sort Fire Radiative Power values and retrieve 10th, 25th, 50th, 75th, 90th, and 99th percentiles to calculate plume top height for each group, step 3: vertically distribute emission for each calculated height and then give corresponding share to each group. The resulting fire emission profile for the model grid would be the integrated emission rate for all the groups at various heights (the black line).

model and updated at each model time step (i.e., 30 min). In addition, we use the retrieved daily observed FRP percentiles as input and do not consider the diurnal variation of FRP.

2.7. Implementing Injection Schemes in AM4.0

After calculating injection height, the emissions are distributed vertically into the appropriate model layers. Similar to Veira, Kloster, Wilkenskjeld, and Remy (2015) we applied a constant mass mixing ratio tendency from the surface to the top of the plume. The inputs fields of the Sofiev scheme include the resampled MODIS FRP from Terra/Aqua, the model PBL height, surface pressure, and temperature profile. Another important aspect of the emission distribution for fires is the sub-grid heterogeneity of fires in each model grid. To consider the heterogeneity of fires within each model grid, we consider FRP values from different percentiles when performing the Sofiev plume height calculation. We used the 10^{th}, 25th, 50th, 75th, 90th, and 99th percentile values to calculate six plume height values and distribute them based on their share from the total grid area (i.e., assuming fires are distributed evenly within each percentile range in a grid cell, the shares are allocated as follows: 10% for the 0–10th percentile, 15% for the 10th–25th percentile, 25% each for the 25th–50th and 50th–75th percentiles, 15% for the 75th–90th percentile, and 10% for the 90th–99th percentile). This is done for each grid cell to achieve a scale-aware distribution of injected aerosols in coarse grid cells of the climate model. Figure 2 shows a schematic of the scale-aware emission distribution process. The implementation in AM4.0 included modifications of the aerosol module to account for plume height calculation and emission distribution.

3. Experimental Design

We conducted a set of sensitivity experiments comparing the default AM4.0 BB plume injection scheme (see Section 2.1), with the Sofiev parametrization with different configurations (see Section 2.6) as well as other parametrizations such as surface injection. The detailed description of each experiment is provided in Table 1. In

Table 1
List of Experiments Using Various Injection Height Schemes and Biomass Burning (BB) Emissions

Experiments	Carbonaceous BB injection	SO_2 BB injection	BB emissions
AM4_default	Fixed height (Dentener et al., 2006)	In PBL	GFED4.1s daily
Sofiev_orig	Sofiev scheme (Equations 1 and 2)		GFED4.1s daily
Sofiev_sfrp	Sofiev + subgrid FRP recalculation (Equation 1 + Equations 5 and 6)		GFED4.1s daily
Sofiev_2step	Two-step Sofiev method (Equations 1–4)		GFED4.1s daily
Surface_inj	Injected to surface layer		GFED4.1s daily
AM4_nofire	No BB injection		No BB emission

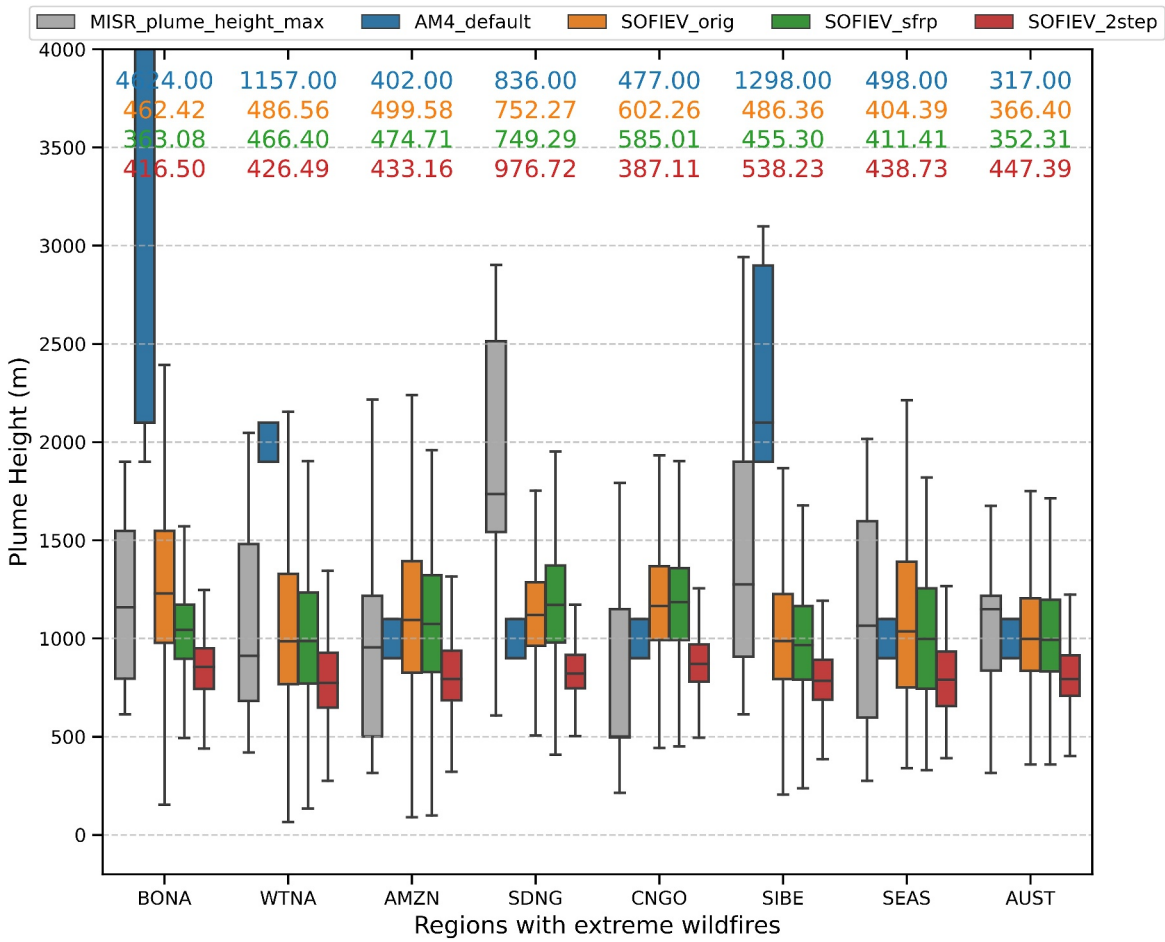

Figure 3. Boxplots of different versions of Sofiev method and default AM4.0 in comparison with MISR plume height project observation data set for each region (numbers on top are median absolute error between injection schemes and observed data set).

this section, we compare the calculated plume height of the different versions of the Sofiev scheme with those from the MISR Plume Height project.

The results are screened to select cases of extreme wildfires, as described in Section 2.2. Figure 3 provides statistics related to plume injection heights for each experiment, and MISR data for the 8 different regions of sustained extreme wildfires (Figure 1). The most striking result is the excessive plume height when using a fixed altitude of injection over high-latitude regions (i.e., BONA, WTNA, SIBE). Beside these regions, most experiments provide results consistent with MISR data, except in Sudan-Guinea region (i.e., SDNG) where MISR has much higher plume heights and spread. Furthermore, the original and sfrp-corrected Sofiev schemes provide similar results, however, the 2-step method (i.e., Sofiev 2-step) systematically underestimates plume height and variability. Achieving better accuracy would require the incorporation of additional factors, such as aerosol absorption (Ohneiser et al., 2023) and convection (Ma et al., 2024), to more effectively capture high-altitude injections (e.g., pyroCbs). Overall, the original Sofiev method covers most of the spread and provides satisfactory agreement with MISR observations. Since the differences between the various Sofiev modifications were minimal, we will only focus on comparing the AM4_default, Sofiev_orig, Surface_inj, and AM4_nofire experiments with observations.

4. Vertical Profiles of Carbonaceous Aerosols

In this section, the 18-year mean vertical profiles of black and OC concentrations from the different experiments are compared. Figure 4 shows concentrations of BC over each BB region. As expected, aerosol concentrations are dramatically higher in all experiments with BB emissions than in AM4_nofire. The differences between injection

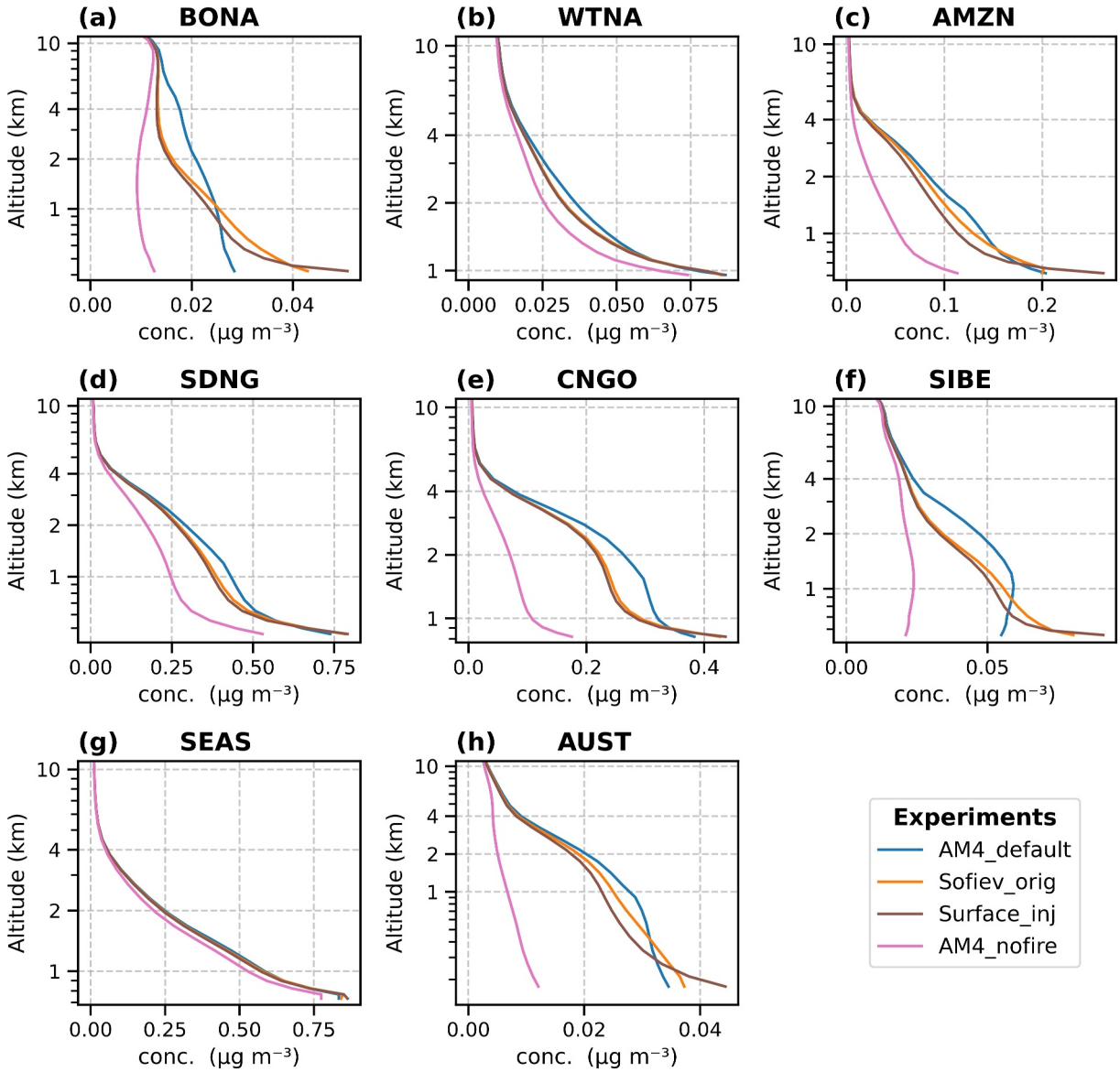

Figure 4. Black carbon concentration vertical profiles for various experiments over extreme wildfire regions.

schemes are also significant at the 90% level in all the regions. This is true for each wildfire region except Southeast Asia for two main reasons: First, the share of fire-emitted aerosols in Southeast Asia compared to anthropogenic aerosols is marginal (Permadi et al., 2018). Second, convective updrafts effectively suck aerosols out of the boundary layer to the upper troposphere where they are transported to downwind regions (Liu et al., 2020; Pouyaei et al., 2021). Implementation of a mechanistic emission distribution changes the vertical profile significantly. The most significant differences are for altitudes below 6 km. Surface injection keeps most of the concentrations near the surface, therefore we see lower concentrations in the free troposphere. The Sofiev experiment shows marginally higher concentrations in the free troposphere than with surface injection but follows a similar profile (as opposed to profiles from fixed injection height in AM4_default). This is because the dynamic injection uses PBL height as an input, and during the nighttime the height of the stable boundary layer is usually close to the surface, while during daytime it doesn't develop extensively over these regions. BB aerosols injected to lower model layers are more likely to be removed by dry deposition. The 18-year mean of various Sofiev parametrizations yields similar vertical profiles of aerosol for most of the regions. The difference between experiments is more dominant in boreal North America, Amazon, Siberia and Australia, with persistent presence of wildfires and greater values of FRP. Organic carbon concentrations show similar profiles as BC with less

variability between experiments (Figure S2 in Supporting Information S1). The weak difference between OC concentrations profiles for various experiments in regions like Amazon, Southeast Asia, and Australia is most likely due to their low share of BB emissions compared to other anthropogenic and biogenic sources. In addition, we compared BC and OC concentrations with Particle Analysis by Laser Mass Spectrometry (PALMS) instrument during the four ATom campaigns from 2016 to 2018 (Figure S3 in Supporting Information S1; Froyd et al., 2021). In our analysis, we found similar profiles for all experiments ($\sim\pm0.1$ μgm^{-3} differences), because first, flight paths were chosen mostly over the ocean to analyze the background concentrations, and second, no extreme BB episodes were sampled during the flights.

5. Aerosol Optical Depth

5.1. Comparison With MODIS AOD

In this section, we evaluate the 18-year mean modeled AOD with MODIS retrieved AOD for different BB injection experiments. Figure 5 shows the 18-year mean of AOD simulated with the original Sofiev scheme (Sofiev_orig), and the difference of AOD across experiments and MODIS retrieved AOD. Panel (a) shows the simulated AOD with Sofiev_orig experiment. The mean AOD in the wildfire regions varies between ~0.15 (Amazon forests) and ~0.27 (Congo forests). The main difference between these results and MODIS observations (Figure 5b) is over Africa where AOD is largely underestimated with a mean bias of −0.34. This is 3 times higher than the global mean bias (−0.09). These underpredictions are mostly attributed to the BB emissions from GFED inventory, as discussed by Pan et al. (2020). Central Africa is also the region with the highest level of AOD (~0.09) associated with BB as shown in Figure 5c. But the contribution of BB to AOD is also apparent in the Amazon forests, Siberia, North America and equatorial Asia, although with lower value around 0.05. Although globally the contribution of BB to total AOD is almost 7%, over tropical forest of central Africa, almost 33% of AOD is from BB (Figure 5c). Figure 5d shows that the main impact on AOD after replacing the injection from surface emission to Sofiev is an overall increase of about 7.2% when comparing to increase from BB emissions. The largest increases are in the tropical forest of South America, South Africa and South-east Asia, with maximum value around 0.01. Such increase may have been significantly higher if not due to the very low bias of GFED BB emission (Pan et al., 2020). Our analysis on the Congo forests and outflow region (Figure S4 in Supporting Information S1) shows that the overall impact of Sofiev scheme is more pronounced if the BB emissions and injection height are simultaneously high (for high FRP values if the emissions were doubled the AOD differences would become at least 30% larger). Figure 5e shows that inaccurate continuous injection of BB emissions to fixed altitudes (as previously discussed in Section 3), increase the lifetime of aerosols globally, especially in BB regions and their downwind areas, leading to negative bias between Sofiev_orig and AM4_default (e.g., Congo and outflow observed almost 6% higher AOD than Sofiev dynamic injection).

Comparing the AOD bias for each experiment relative to MODIS data as a function of FRP shows a systematic dependency of bias under conditions with large FRP values (Figure S5 in Supporting Information S1). Over tropical Africa, we see a sudden large increase of bias (~0.2) similar for all experiments when FRP is greater than 1 GW. To a much less extent, similar increase of bias for high FRP appears in Southeast Asia and Australia. In addition, all statistical measures of bias are almost identical between experiments. This indicates that AOD bias is weakly related to the injection scheme and the large uncertainty in simulated AOD is due to the fire emission inventory bias.

5.2. Comparison With AERONET AOD

With direct measurement of AOD by sun photometers, the estimated error of AOD from AERONET is at least half the error associated with MODIS retrievals. Comparison with AERONET data provides more accurate comparison but is representative of a limited area. This section focuses on comparing seasonal variation of AOD at the AERONET sites located in the extreme wildfire regions (Figure S6 in Supporting Information S1). Figure 6 shows the AOD bias for three experiments and for two extreme wildfire seasons per region. Overall, the Sofiev scheme largely decreases the different statistical measures of bias relative to methods using fixed injection height, either at the surface (Surface_inj) or at different altitudes (AM4_default). The comparison is quantified in Table 2, showing that the Sofiev scheme has a lower absolute median bias (0.059) than others (0.064–0.065). The largest bias in Figure 6 is associated with wildfires in the North America boreal forests during summer 2017. The record-breaking 2017 summertime wildfire season in Canada, with more than 9,000 square kilometers burned (Coogan

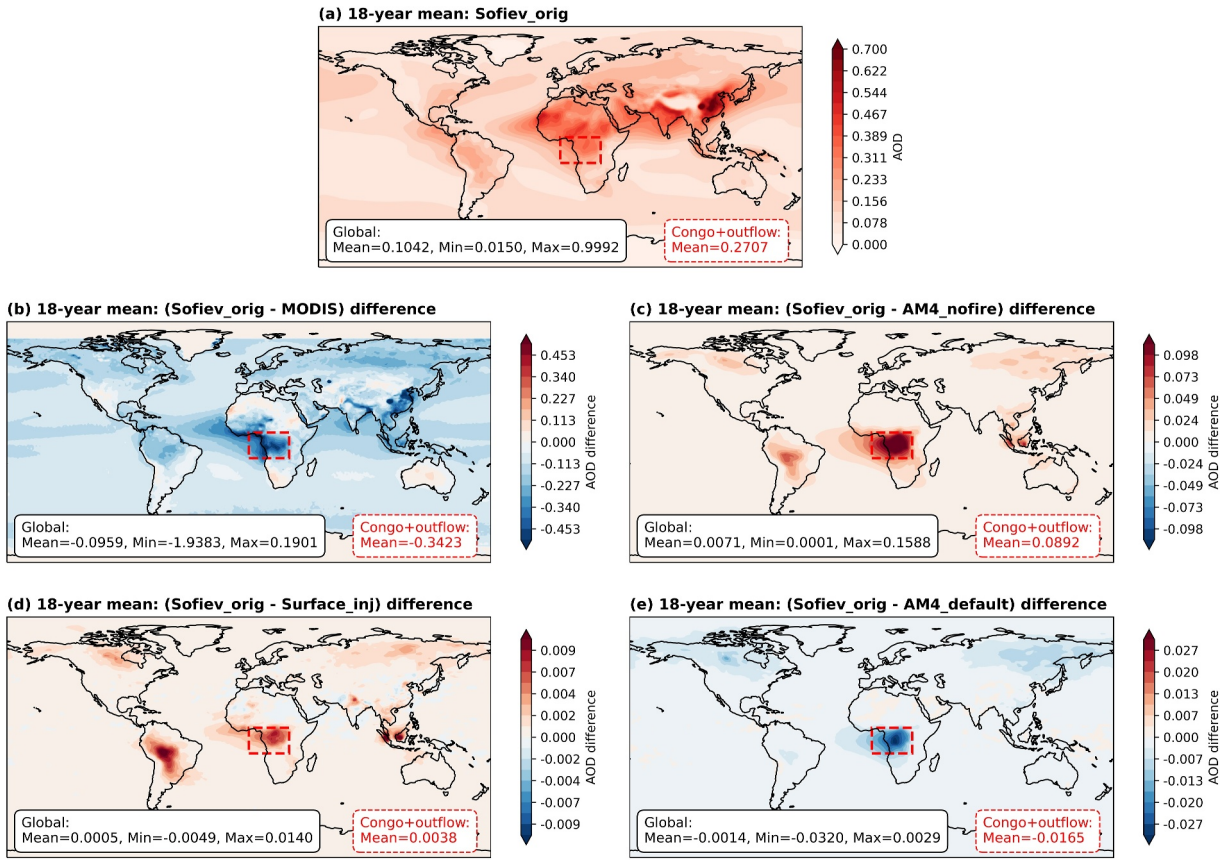

Figure 5. 2003–2020 averaged aerosol optical depth comparison between experiments and observation: (a) Sofiev_orig experiment; (b) the difference between Sofiev_orig and MODIS measurements; (c) The difference between Sofiev_orig and AM4_nofire experiment; (d) the difference between Sofiev_orig and Surface_inj; and (e) the difference between Sofiev_orig and AM4_default. The left corner box shows mean, minimum and maximum values for globe, and the right corner dashed red box shows the mean value for Congo forests and outflow region.

et al., 2019), observed an extremely large reduction in AOD bias by Sofiev injection (median difference of −0.5). Depending on the accuracy of BB emissions, the Sofiev injection scheme tends to reduce the biases. The reduction in bias is evident in all regions while comparing Sofiev with Surface injection. However, in the case of the 2020 extreme Australian wildfires, there is the conjunction of a large overestimation of BB emission and slight positive bias of Sofiev scheme. For the two most extreme wildfire seasons in all the regions (shown in Figure 6), the Sofiev scheme similarly produced better estimations of AOD with biases 10% lower than AM4_default (0.105 compared to 0.114). The contribution of aerosol species to total AOD for the extreme wildfire seasons in each region (Figure S7 in Supporting Information S1) shows a significant amount of AOD is attributed to primary organic aerosol and sulfate, and then SOA. Minor fractions of BC (below 5%) are observed in boreal North America, Amazon, Sudan Guinea, Congo, Southeast Asia, and Australia. In our simulations, total AOD over Australia is dominated by dust during the extreme wildfires (possibly one of the reasons for opposite response in reducing AOD bias of this region). The selected Australian domain includes multiple sources of aerosol but is dominated by dust and BB aerosols. The dry season in Australia is also the period of intense dust activity around the Lake Eyre region, while wildfires are essentially located in northern Australia (Yu & Ginoux, 2021).

6. Vertical Profiles of Aerosol Extinction

In this section, we analyze the vertical profile of the aerosol extinction coefficient from each experiment and compare it to CALIOP observations and examine the global spatial distribution of extinction-weighted aerosol heights, as a metric for aerosol vertical distribution after Koffi et al. (2012). To ensure a robust comparison and to focus our analysis on BB-derived aerosols, we select the daily vertical profiles from the model corresponding to extreme wildfire events (wildfires with at least five continuous days of 99th percentile of FRP values above

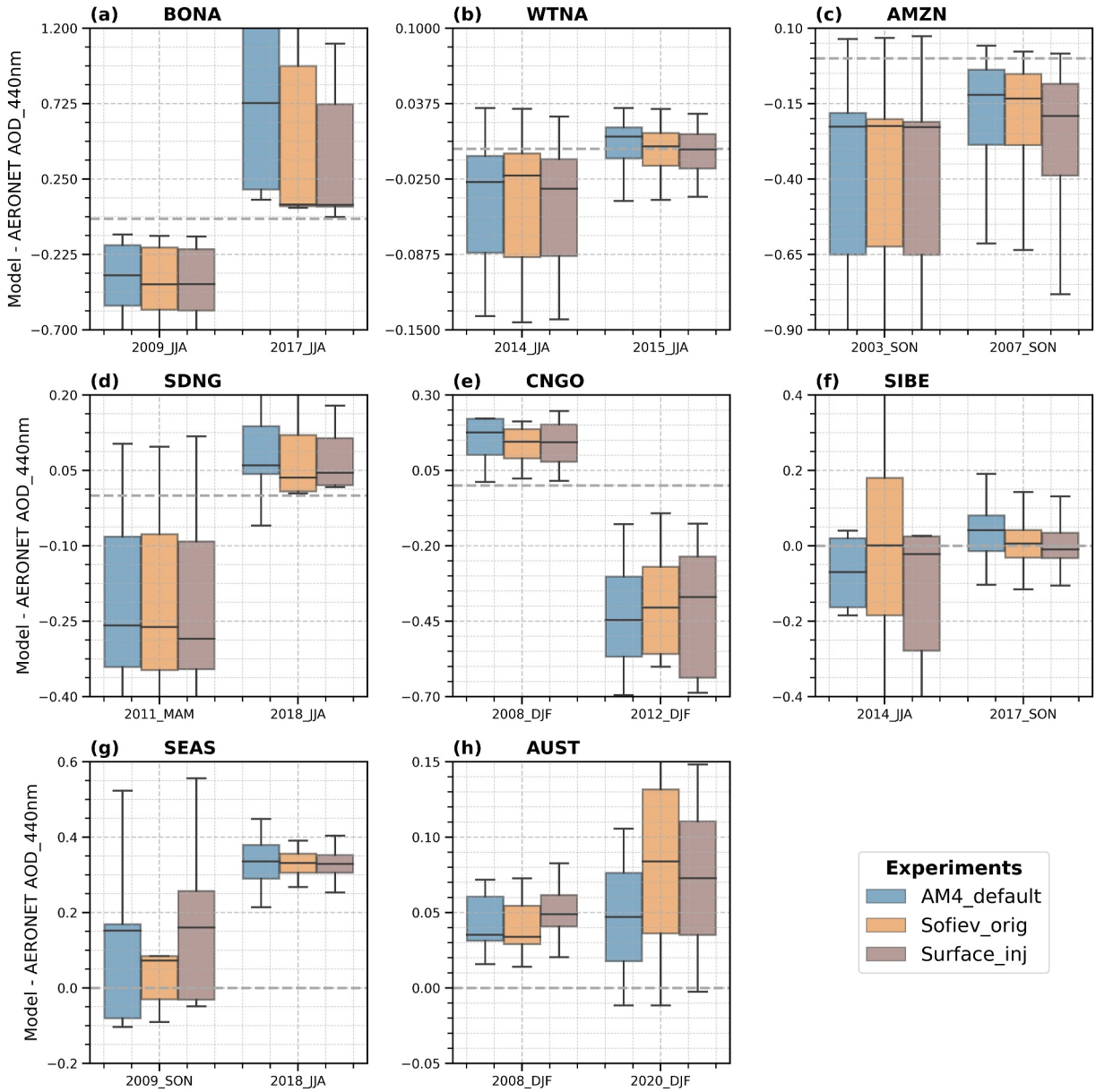

Figure 6. Simulated Aerosol Optical Depth bias, relative to AERONET sun photometer data, for three experiments and during two extreme seasons over eight sustained wildfire regions.

Table 2
Statistical Analysis of Biases for Modeled Aerosol Optical Depth (AOD) Versus AERONET AOD for Extreme Wildfires Seasons

Experiment	Absolute median bias of 2003–2018 extreme seasons per region (not shown)	Absolute median bias of the two most extreme seasons per region (as shown in Figure 6)
AM4_default	0.065	0.114
Surface_inj	0.064	0.118
Sofiev_orig	0.059	0.105

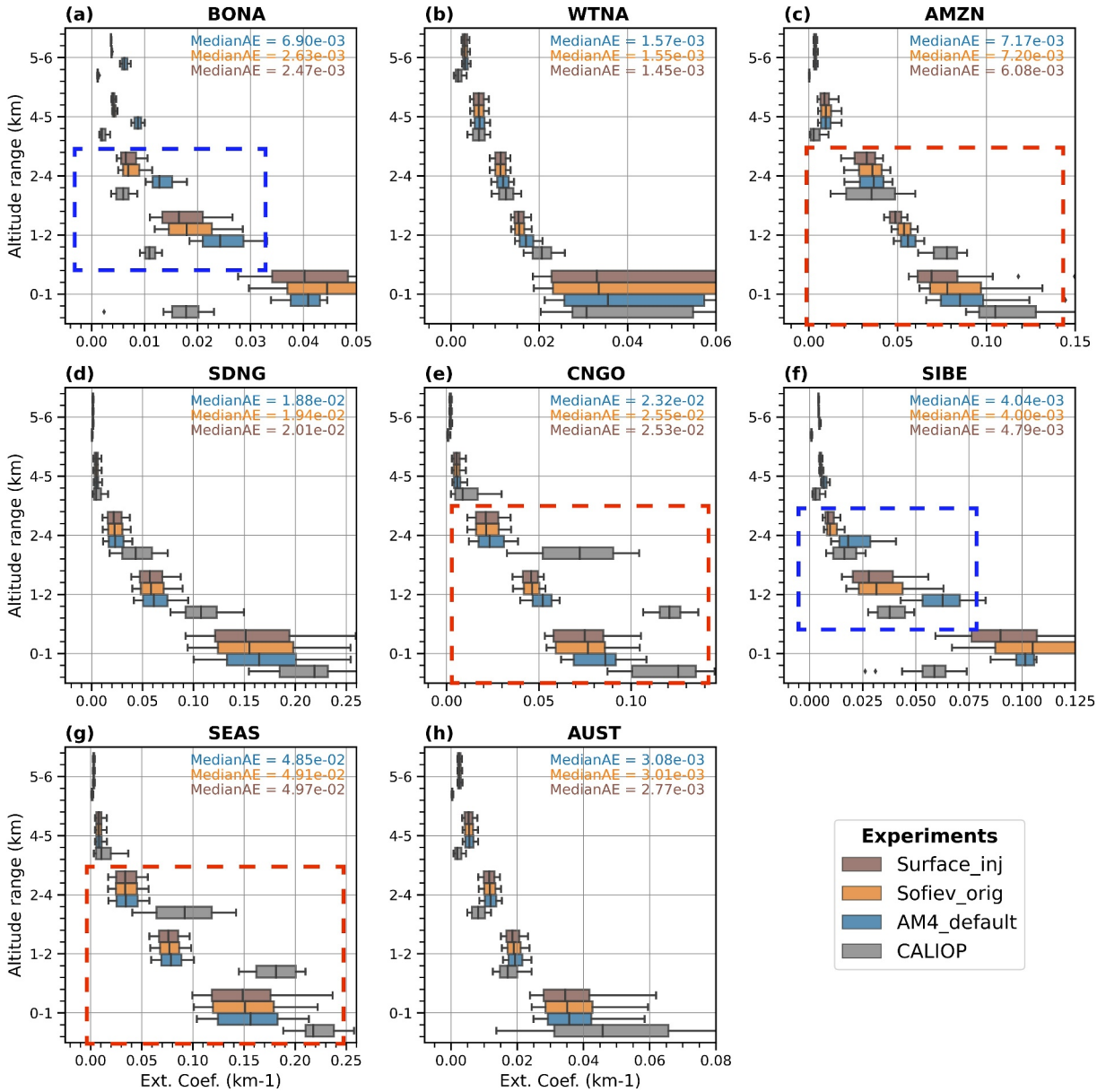

Figure 7. Vertical profiles of extinction coefficient (km^{-1}) from the surface to 6 km altitude from three experiments and Cloud-Aerosol Lidar with Orthogonal Polarization measurements collocated in time and averaged over 8 sustained wildfire regions.

500 MW). Figure 7 shows the extinction profiles of three experiments and CALIOP observations over the eight selected wildfire domains. Near the surface, the bias is the largest without indication of systematic bias. The largest biases are over the boreal forest of North America (panel a) and Siberia (panel f) especially in lower altitudes (less than 4 km). The almost 50% reduction in bias in the Sofiev experiments versus AM4_default over boreal regions (shown with blue dashed box in panels a and f) in the free troposphere between 1 and 4 km altitude is attributed to the Sofiev parametrization's ability to inject the aerosols to the correct altitude. Western temperate North America, East Africa, and Australia share a smooth profile following the CALIOP observations (panels b, d, and h). However, Congo, Southeast Asia, and partly Amazon, show a bell-shaped profile for CALIOP compared to smooth model profiles (shown with red dashed box in panels c, e, and g). The difference between model and observation in the mentioned regions is rooted in the complexity of cloud processes (e.g., model's positive bias in precipitation leads to higher washout of aerosols) and of the secondary aerosol formation (e.g.,

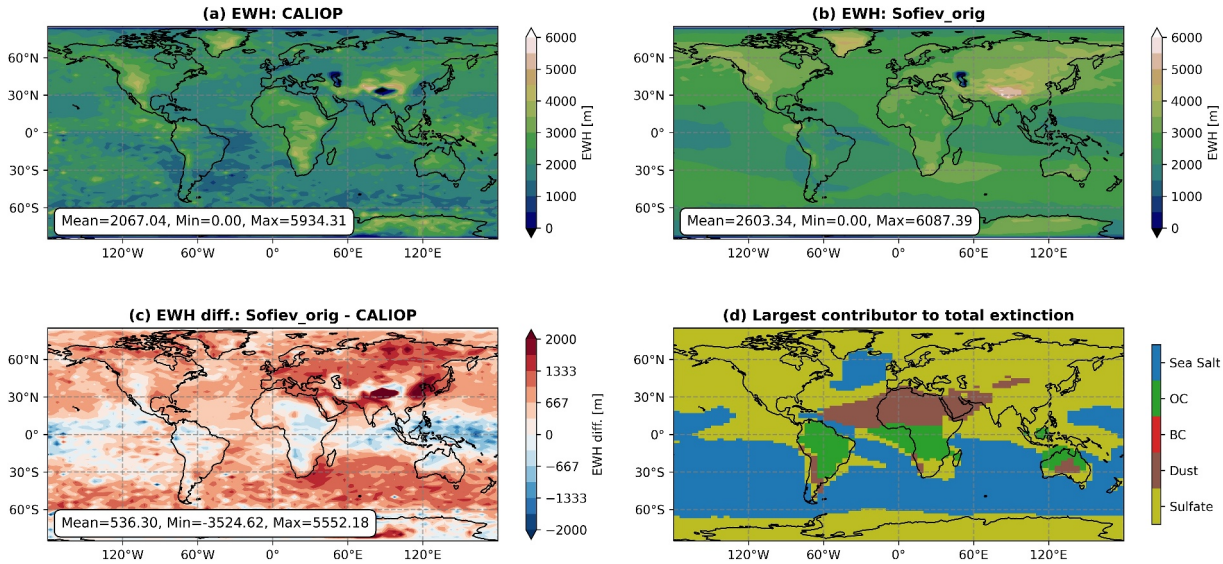

Figure 8. Extinction-weighted height (EWH) calculated by (a) the Cloud-Aerosol Lidar with Orthogonal Polarization 532 nm extinction profiles, (b) the Sofiev_orig experiment, and (c) EWH difference between Sofiev_orig and CALIOP; The largest contributor to total extinction is shown in panel (d). The statistics provided are global mean (Mean), minimum (Min) and maximum (Max). Units are in meters.

model neglects the effect of variable oxidant levels on both reaction rates and yields of SOA formation) (Andreae et al., 2001; Guo et al., 2021; Kelly et al., 2018; Koffi et al., 2012).

To analyze the spatial distribution of aerosol vertical profiles, Koffi et al. (2012) suggested the use of extinction-weighted height (EWH), which was later adopted by multiple studies (e.g., Chimot et al., 2018; Liu et al., 2019; Nanda et al., 2020). EWH is the mean of aerosol layer height weighted by the extinction of each layer. It represents a characteristic height of the column AOD, and is given by the following equation,

$$\mathrm{EWH} = \frac{\sum_{i=1}^{n} \beta(z_i) \cdot z_i}{\sum_{i=1}^{n} \beta(z_i)} \tag{7}$$

where $\beta(z_i)$ is the aerosol extinction coefficient at vertical layer defined by its mid-altitude, z_i. Figure 8 panels (a) and (b), shows EWH extracted from CALIOP retrieval and the Sofiev experiment. We focused on EWH extracted from 0 to 6 km altitude, because most of the aerosol load is concentrated in this altitude range. Furthermore, the CALIOP instrument systematically misses high-altitude aerosols (also shown in Figure 7) due to its extinction coefficient detection limit of ∼0.01–0.015 km^{-1} (Koffi et al., 2012). The model overestimates EWH by ∼600 m on average compared with CALIOP consistent with the previously reported ∼1 km overestimation of EWH from AeroCom models (Koffi et al., 2012). There is a clear meridional variation with negative bias in the tropics changing to a positive bias when moving to higher latitudes. The positive bias in northern hemisphere (which is largely contributed by sulfate extinction, Figure 8d) is mainly due to a combination of too effective vertical mixing (either from low vertical resolution or from convective mixing), and too little removal of aerosols. The positive bias in EWH over the ocean is largely contributed by sea salt which is missed by CALIOP-derived aerosol extinction profile due to inherent limitations and uncertainties in measurements (Figure 8d). The negative bias in BB regions (such as Congo and northern Australia) could be explained by emission inventory bias and potentially low secondary aerosol formation, which was also observed from the discrepancies in the shape of vertical extinction profiles in Figure 7. Furthermore, the negative biases in EWH (Figure 8c), which predominantly coincide with regions where OC/BC are the largest contributors to total extinction (Figure 8d), are also located in equatorial areas characterized by high convective activity. This overlap suggests that a combination of biases in emission inventories and inaccuracies in convective processes and precipitation (Guo et al., 2021; Zhao et al., 2018a) may prevent aerosols from reaching higher altitudes or may remove them through wet-deposition process, thereby reducing their atmospheric lifetime and resulting in lower EWH values.

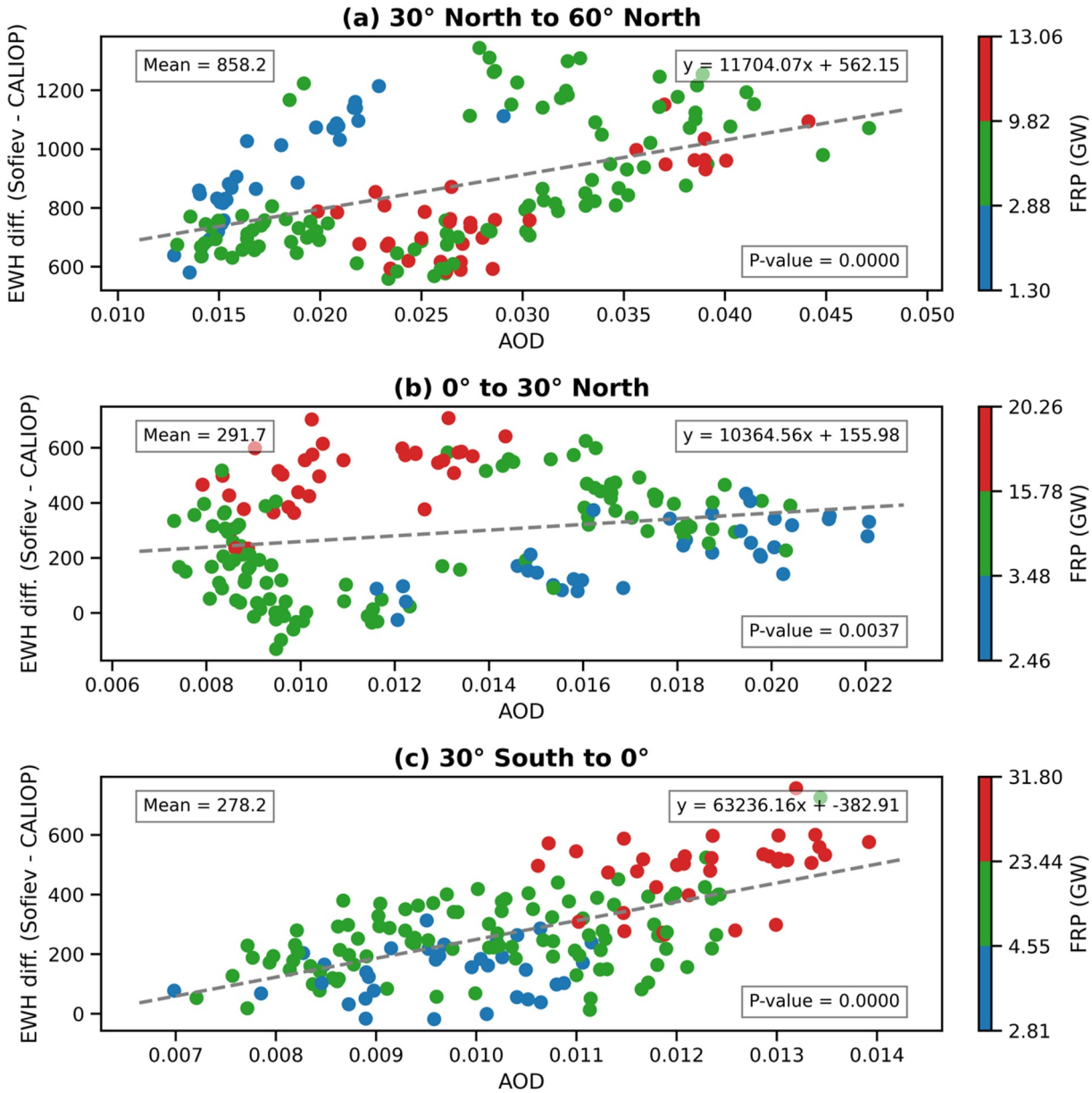

Figure 9. The relationship between extinction-weighted height difference of Sofiev method and Cloud-Aerosol Lidar with Orthogonal Polarization observations (*y*-axis) with monthly mean Aerosol Optical Depth values (*x*-axis) and monthly fire radiative power values (colorbar) for three globally averaged latitude ranges: (a) 30° North to 60° North, (b) 0°–30° North, and (c) 30° South to 0°.

To better understand the meridional variation of EWH bias, the EWH difference is plotted as a function of AOD and by range of FRP over 3 regions: 30°–60° North (NH mid-latitudes), equator to 30° North (NH tropics), and 30° South to equator (SH tropics). In NH mid-latitudes and NH tropics (Figures 9a and 9b), the higher the AOD, the higher is the bias. The relationship appears to be independent of FRP intensity and can be attributed to the significant contribution of anthropogenic and dust aerosols in these regions (Figure 8d). On the other hand, the EWH difference in the SH tropics (Figure 9c), which is mostly contributed by BB aerosols (Figure 8d), is lower (mean ∼278 m compared to ∼858 m in NH mid-latitudes) and low/high FRP values are clustered. Comparing the values categorized by the regions with the largest contributor to total extinction (Table S1 in Supporting Information S1) also shows that BC/OC dominant region have the lowest bias and highest FRP. Results from this analysis further confirms that uncertainties in the BB inventory affect not only the aerosol load but their vertical profile, and consequently their lifetime in the atmosphere.

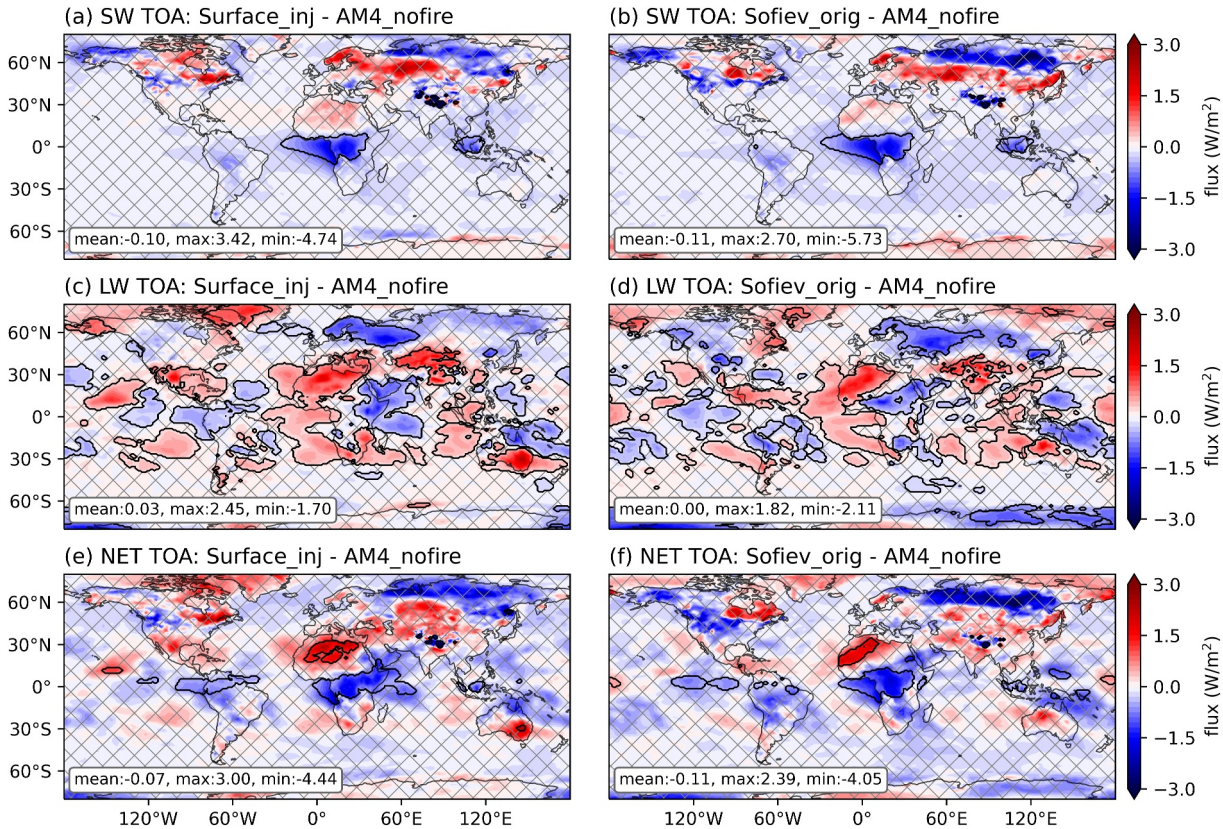

Figure 10. Clear-sky radiative flux anomalies (shortwave/SW: first row; longwave/LW: second row; NET: third row) at top-of-the-atmosphere (TOA) with AM4_nofire as control experiment for Surface_inj experiment (panels a-c-e) and Sofiev_orig experiment (panels b-d-f). Hatched area are insignificant points according to 90% significance level. The statistics provided in the lower left corner are global mean values.

7. Radiative Impacts of Biomass Burning Injection

Introducing BB injection schemes into the AM4.0 climate model affects the aerosol optical properties as previously discussed, therefore affecting the radiative budget through shortwave (SW) and longwave (LW) interactions. Here, we analyze the radiative impacts of the surface injection and Sofiev injection on the radiation budget relative to the case of AM4.0 without BB emissions (AM4_nofire). This analysis will provide the overall radiative impact from BB aerosols with surface injection in the climate model (Surface_inj minus AM4_nofire), and radiative impact from BB aerosols with dynamic injection (Sofiev_orig minus AM4_nofire). The simulations in this section are free running simulations (18-year simulations without nudging, using similar inputs and configurations as those discussed previously) to assure the consistency between fast atmospheric and land response. We focus on clear-sky (free of clouds) radiative fluxes for SW, LW, and NET (SW + LW) for more clarity, focusing on direct rather than indirect radiative effects from BB aerosols.

Figures 10 and 11 show the anomalies in radiative fluxes (SW, LW, and NET) under clear-sky conditions between Surface_inj and AM4_nofire (panels a-d-g) and between Sofiev_orig and AM4_nofire (panels b-e-h) at top of the atmosphere (TOA) and surface (SFC), respectively. Hatched lines show anomalies which are statistically non-significant (below 90% significance level based on the Student's t test). The regions with significant clear-sky SW radiative perturbations at TOA due to BB are limited to tropical Africa and Southeast Asia. The clear-sky SW radiative cooling from BB aerosol emission is of the order of -1.5 Wm^{-2} in those regions, with either surface injection or dynamic vertical injection. No other regions show significant response in clear-sky radiative fluxes. Presence of BB smoke aerosols results in decrease of sunlight shortwave radiation reaching to the ground, which leads to a cooling effect near and downwind of BB regions (Li et al., 2022). On the other hand, longwave forcing has more significant points, usually with an opposite sign compared to SW. The clear-sky radiative effect anomaly associated with dynamic injection shows a more negative LW flux largely in boreal North America, boreal Asia, equatorial Asia, and central Africa. The region with the most anomalous positive difference from dynamic

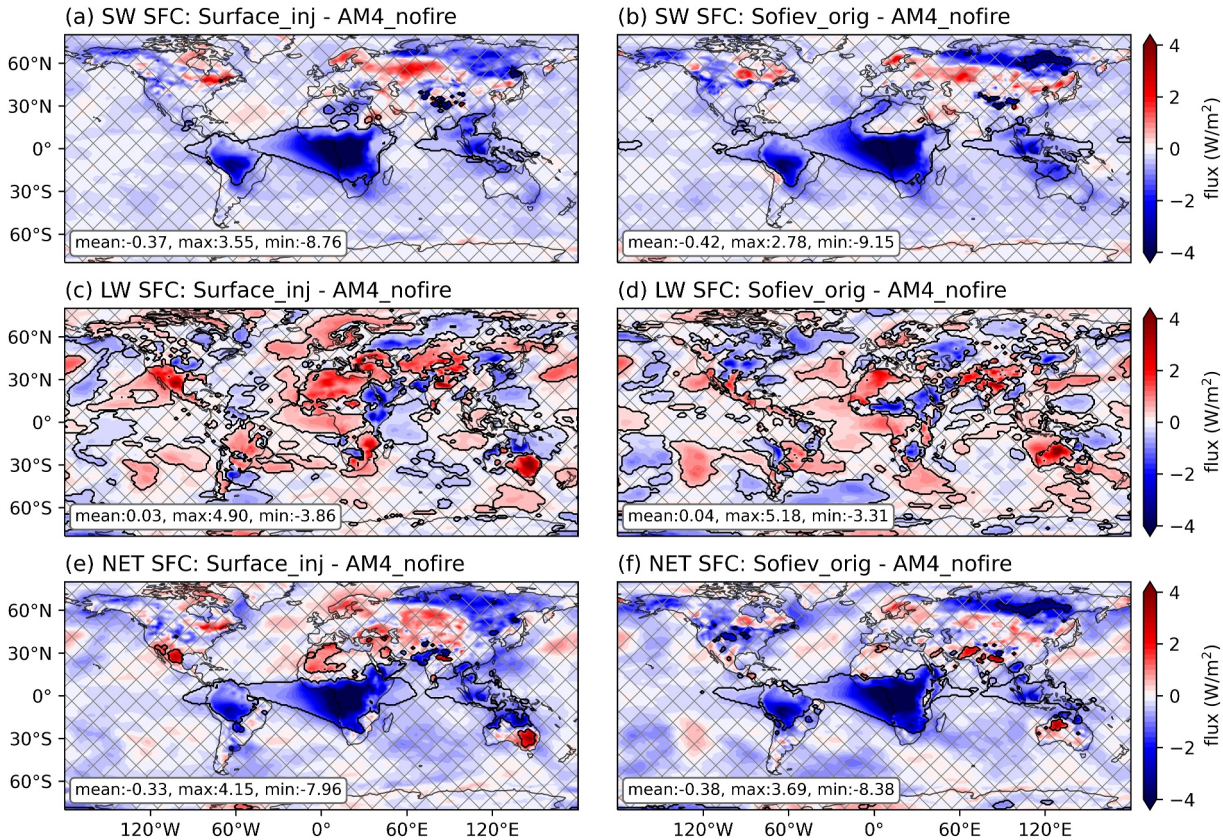

Figure 11. Clear-sky radiative flux anomalies (shortwave/SW: first row; longwave/LW: second row; NET: third row) at surface (SFC) with AM4_nofire as control experiment for Surface_inj experiment (panels a-c-e) and Sofiev_orig experiment (panels b-d-f). Hatched area are insignificant points according to 90% significance level. The statistics provided in the lower left corner are global mean values.

injection are northern Africa, South Asia, and northern Australia. The anomalies in clear-sky radiative flux at the TOA (Figure 10) show a strong correlation with changes in aerosol optical depth (AOD; Figures S8b and S8c in Supporting Information S1). Biomass burning (BB) emissions release both absorbing aerosols, such as BC, and scattering aerosols, including OA and sulfate, into the atmosphere. These aerosols influence atmospheric circulation patterns, such as near-surface wind strength and direction, and contribute to changes in dust loading. In wildfire regions, AOD anomalies are predominantly driven by OA, followed by sulfate and BC, while in the Sahara, dust aerosols dominate (Figure S9 in Supporting Information S1). The increased loading of BB and dust aerosols enhances both the absorptivity (i.e., increase absorption AOD as shown in Figures S8e and S8f in Supporting Information S1) and the AOD of the atmosphere (Figures S8b and S8c in Supporting Information S1). However, the net radiative effect under clear-sky conditions also depends on the surface albedo of the regions where aerosols are distributed. Over the Saharan desert, the increase in AOD leads to a warming effect (Figures 10e and 10f) due to the darker appearance of absorbing aerosols over the highly reflective desert surface (Li et al., 2022; Thorsen et al., 2020). Conversely, in BB regions, increased AOD results in negative clear-sky radiative effects (cooling). This follows the general principle that higher AOD is associated with greater aerosol-induced cooling (Thorsen et al., 2020). Moreover, the changes in clear-sky direct radiative effects in high latitude regions (e.g., Siberia) are correlated with the changes caused by BB aerosols to surface albedo (Figures S8h and S8i in Supporting Information S1). Overall, the Sofiev_orig anomaly showed -0.11 Wm^{-2} in global mean NET clear-sky TOA effect versus AM4_nofire, compared to an anomaly of -0.07 Wm^{-2} from Surface_inj, indicating an overall cooling response from wildfires and a larger cooling response from dynamic injection compared to surface injection.

Backscattering and absorption by BB aerosols reduce SW fluxes at the surface, causing a significant cooling at the surface (see BB regions in Figures 11a and 11b). The cooling effect from dynamic injection is stronger in Indonesia (possibly because combination of higher injection heights and strong convective updrafts in this region increases BB aerosols lifetime in the atmosphere) and Siberia (due to increase in surface albedo, compare Figures

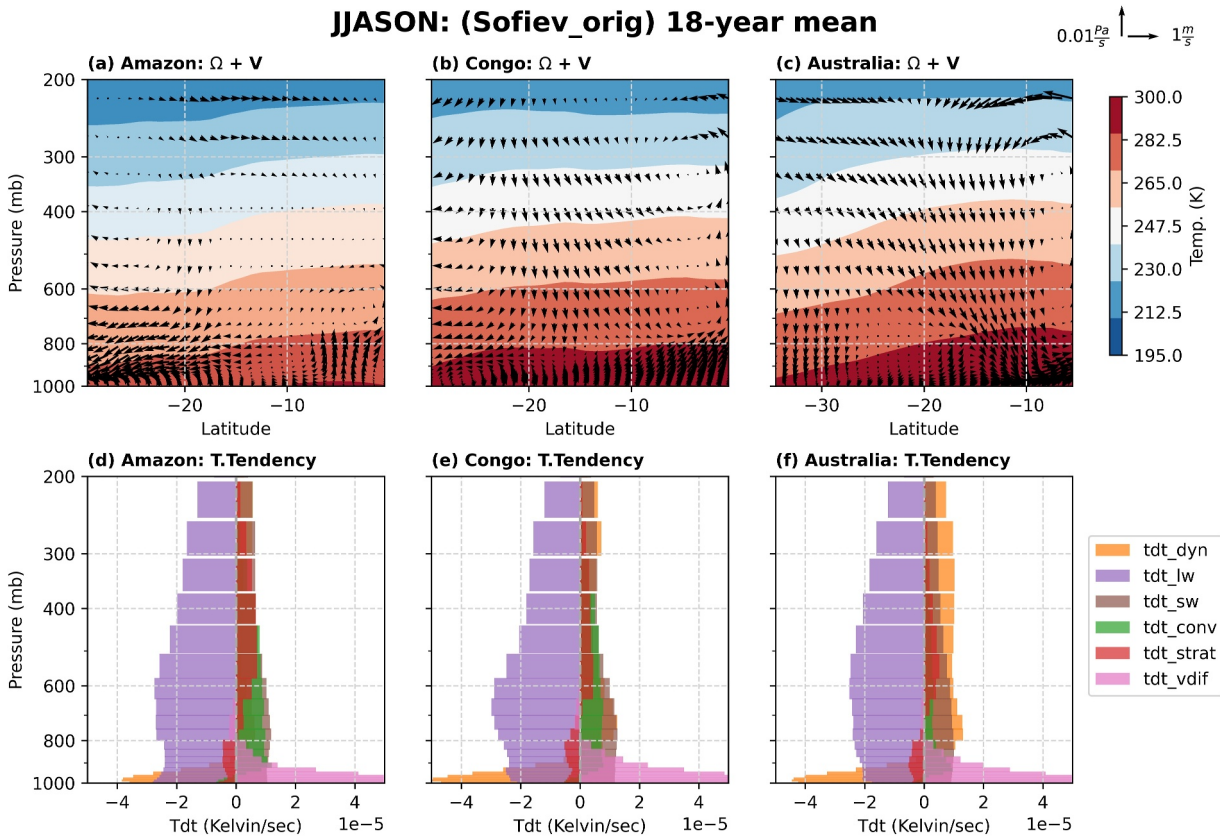

Figure 12. First row: Zonally averaged vertical velocity ($-dp/dt$) and meridional winds overlayed by temperature difference for (a) Amazon, (b) Congo, and (c) Australia. Second row: Temperature tendency from model processes including dynamics (tdt_dyn), convection (tdt_conv), stratocumulus clouds (tdt_strat), shortwave radiation (tdt_sw), longwave radiation (tdt_lw), vertical diffusion (tdt_vdif), and other physical processes (tdt_othr) for (d) Amazon, (e) Congo, and (f) Australia. All variables are the 18-year fire season (JJASON) mean of the Sofiev_orig model experiment.

S8h and S8i in Supporting Information S1). The clear-sky LW anomalies have similar patterns for both experiments with opposite sign in most regions inside the equatorial zone. NET SFC clear-sky global mean flux indicates stronger cooling over surface for dynamic injection (-0.38 Wm^{-2}) compared to surface injection (-0.33 Wm^{-2}). Major BB regions, such as Congo forests, boreal Asia, and Amazon forests have a NET cooling effect at the land surface, indicating an increase in low-level thermodynamic stability (Randles & Ramaswamy, 2010). Interestingly, as opposed to other major BB regions, northern Australia shows a different pattern in the Sofiev experiment (a positive NET surface radiative flux). The all-sky radiative fluxes for TOA and SFC are also presented in Figures S10 and S11 in Supporting Information S1 for reference (supplement document). The all-sky SFC flux anomalies show more pronounced differences between the two experiments in the northern Australia region affecting temperature profiles in the atmosphere. The seasonal variation in AOD, absorption AOD (AAOD), surface albedo, and clear-sky TOA net radiative flux, as shown in Figure S12 in Supporting Information S1, highlights how the region and strength of fire aerosols' influence on the atmosphere vary across seasons. Examining AOD and AAOD indicates that the strongest impacts occur in June–July–August for boreal regions, the Congo region, and the Amazon, whereas September–October–November shows significant effects in the Amazon, Equatorial Asia, and Northern Australia. Analyzing the climate response to fires by averaging data from June to November provides a clearer picture of the strong direct impacts of fire aerosols, which will be explored in the next section.

8. Climate Response to Biomass Burning Injection

In this section, we investigate the climate response to radiative perturbations due to BB aerosols using Sofiev injection scheme. Figure 12 shows the fire season (June, July, August, September, October, and November) mean state of the zonally averaged meridional circulation pattern, temperature, and temperature tendency profiles over

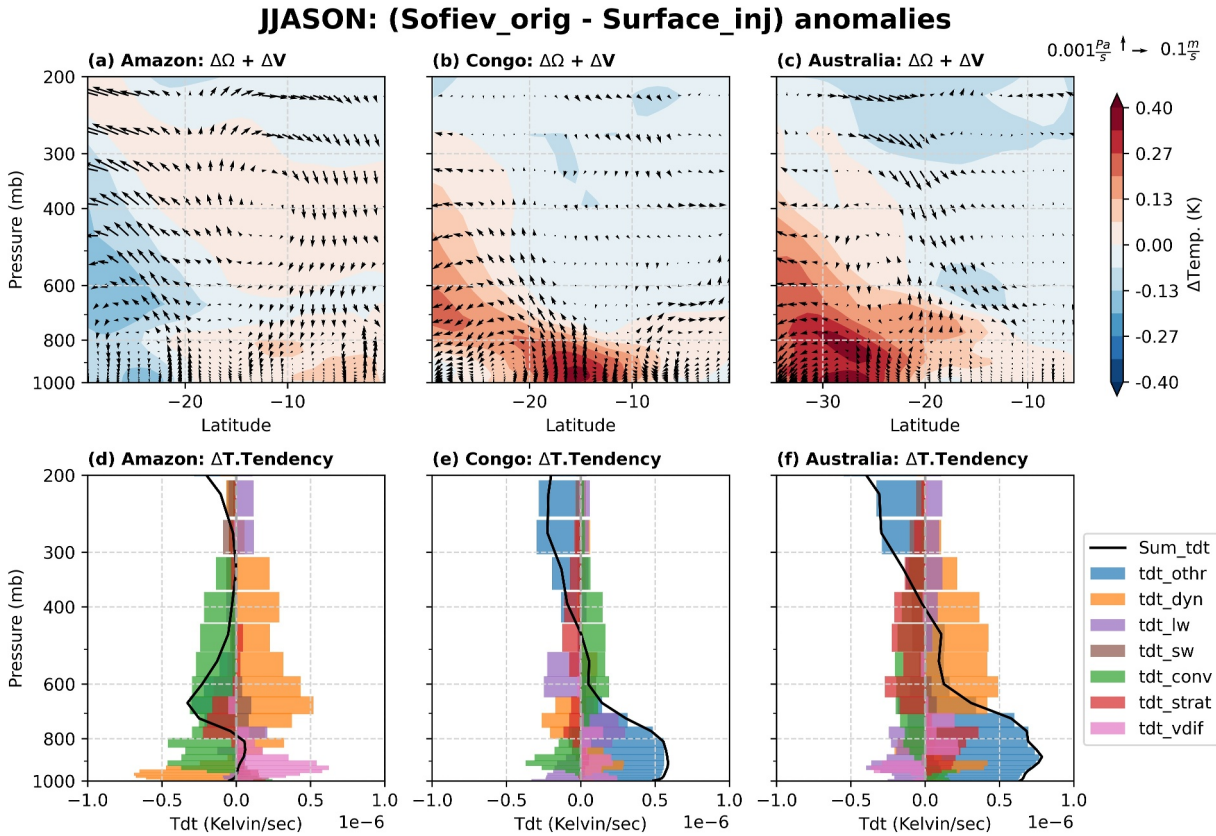

Figure 13. First row: Zonally averaged change in vertical velocity ($-dp/dt$) and meridional winds overlayed by temperature difference for (a) Amazon, (b) Congo, and (c) Australia. Second row: Temperature tendency difference from model processes including dynamics (tdt_dyn), convection (tdt_conv), stratocumulus clouds (tdt_strat), shortwave radiation (tdt_sw), longwave radiation (tdt_lw), vertical diffusion (tdt_vdif), and other physical processes (tdt_othr) for (d) Amazon, (e) Congo, and (f) Australia. All variables are the 18-year fire season (JJASON) mean for difference between Sofiev_orig and Surface_inj experiments.

three regions: Australia and the Amazon and Congo forests. We focused on the average of the specified months, as these months exhibit the most significant impact from fire aerosols (Shown in Figure S12 in Supporting Information S1).

The ascending portion of the Hadley circulation is positioned at different latitudes for each region, and it varies meridionally throughout the year. The upward motion of air due to convergence near the equator and descent at 10°–30° South are observed. The mean state of circulation patterns and temperature are similar for the three regions. The second row of Figure 12 shows the corresponding regionally averaged fire season mean state of temperature tendency. The temperature tendency refers to the mean rate of temperature change for each of the following process simulated by the model at each time step (30 min): Shortwave (*tdt_sw*) increases temperature in all levels due to absorption; Longwave (*tdt_lw*) decreases temperature in all levels cooling down Earth's atmosphere by emitting radiation to outer space; Vertical diffusion (*tdt_vdif*) plays an important role close to surface by mixing the positive heat exchange from surface to the atmosphere; Convective clouds (*tdt_conv*) always increase the temperature by the heat release from condensation process; Stratocumulus clouds (*tdt_strat*) increase the temperature in the middle to upper troposphere due to heat release but decrease temperature by evaporation in the lower troposphere; and lastly dynamics (*tdt_dyn*) decreases the temperature near the surface while increases the temperature in higher altitudes reflecting the adiabatic cooling/warming associated with ascent/descent.

Figure 13 is similar to Figure 12, but it represents the anomalies between Sofiev_orig and Surface_inj experiments during the fire season. This figure aims to identify the dominant processes driving changes in circulation patterns and diagnose the mechanisms behind changes in atmospheric temperature when fire aerosols are dynamically emitted in various altitudes compared to emissions at the surface. We specifically focused on the fire season because the strongest direct impacts of fires on the climate are observed during these months (see Figure S12e and 12i in Supporting Information S1). Over the Amazon forests, a weak negative temperature anomaly is

observed from ∼400 to ∼1000mb in 20°S–30°S latitude range, while in Congo region a strong positive temperature anomaly is observed between ∼400 and ∼800mb in 20°S–30°S range, as well as near the surface in 10°S–20°S range (Figures 13a and 13b). The wind anomalies in both the Amazon and Congo regions oppose the Hadley cell's circulation patterns, with the Amazon displaying a stronger wind anomaly signal. Over Australia, a more pronounced temperature anomaly of 0.5 K is observed near the surface at 25°S–30°S range, extending to higher altitudes, up to ∼500mb at 30°S (Figure 13c). In fact, this large temperature gradient induces an upward vertical motion response, invigorating the descent portion of Hadley cell circulation. The large anomaly in vertical motion could also be an indicator for the instability of the environment in this region. The temperature tendency anomaly for Amazon at different pressure levels (Figure 13d) shows that dynamic injection of fire aerosols reduces convective and stratocumulus clouds, leading to less heat release from cloud condensation process (cooling). It also increases the cooling effect from longwave between ∼800 and ∼400mb, while causing a warming effect from dynamic processes. Near the surface, stronger ascent (cooling from dynamics) and increased vertical diffusion of surface heat are observed. Overall, the profile indicates a cooling response in the atmosphere due to dynamic injection. Conversely, the overall temperature tendency anomaly for the Congo region shows a weak cooling response from dynamic injection at TOA and a strong warming response at lower atmospheric level (Figure 13e). Dynamic injection of fire aerosols in the Congo reduces stratocumulus clouds throughout the atmosphere and convective clouds near the surface while enhancing high-altitude convection. The pattern of temperature tendency change for longwave radiation highlights the effects of dynamic injection on the aerosol profile in the atmosphere. Near the surface and at very high altitudes, *tdt_othr* signals dominate, representing other processes in the model that influence temperature, such as atmospheric turbulent processes. On the other hand, Australia shows slightly stronger response from processes in terms of magnitude (Figure 13f). Vertical diffusion cools the atmosphere meaning less mixing of the heat flux near the surface. Reduced convective and stratocumulus clouds cool the atmosphere, while near-surface stratocumulus clouds contribute to warming. The low-level positive anomaly (warming) for stratocumulus clouds is an indication of less heat consumption by evaporation. Indeed, high injection of BB aerosols in this region reduced the convective activity and cloud cover, as well as shortwave absorption and longwave cooling in higher altitudes. Other processes, such as turbulent processes in the PBL, contribute to increased near-surface temperature. Positive anomalies for dynamics in the ∼700–∼300mb altitude range reflect how vertical and horizontal air parcel movements contribute to warming, demonstrating the compensatory effects of winds in this region. The injection of more BB aerosols to higher altitudes in Australia results in pronounced heating effects. This mechanism affecting temperature profile in southern hemisphere is consistent for all other BB regions and it is largely dependent on the state of cooling/warming at the surface, cloud cover, and circulation patterns in the region.

9. Summary and Conclusions

In this study, we replaced the fixed BB injection scheme of Dentener et al. (2006) in GFDL's AM4.0 model with an implementation of various injection schemes, including Sofiev's deterministic scheme. Using MODIS FRP data, we selected eight regions with sustained extreme wildfires which provide a strong signal to compare each scheme with observations. The BB emission of aerosols is driven by the time series of GFED4.1s emission inventory. The dynamic Sofiev scheme is driven by simulated atmospheric stability and observed FRP from MODIS data. For comparison with observations, the GFDL AM4.0 model is run for 18 years (2003–2020) in AMIP mode with winds nudged toward NCEP reanalysis. The overall comparison of calculated injection heights from Sofiev methods with plume heights observed from MISR data showed a median absolute error less than 500 m in most wildfire regions. This result indicates the scheme's robustness in simulating wildfire plume dynamics. The vertical profiles of carbonaceous aerosols showed relatively marginal differences in various altitudes. The major uncertainty appears in the comparison of AOD with MODIS observations where AOD over Africa and East Asia is largely underestimated. Further analysis of AOD bias reveals that it is only weakly related to the injection scheme but strongly related to BB emission being underestimated by the GFED4.1 inventory. Overall, the Sofiev scheme largely decreases the model bias relative to AERONET sunphotometer data compared to methods using fixed injection height, either at the surface (Surface_inj) or at different altitudes (AM4_default). The comparison of extinction profiles showed that use of the Sofiev scheme reduces model bias by up to almost 50% over boreal regions in the free troposphere between 1 and 4 km. In addition to testing various injection height methods (i.e., Sofiev_orig, Surface_inj, and AM4_default), we conducted an experiment without fire aerosol emissions (AM4_nofire) to isolate the specific effects of fire emissions on aerosol profiles and climate. Lastly, the quantitative analysis of radiative impacts of injection height schemes showed a significant impact on regional and

local climates, affecting the temperature profiles and vertical motion. The dynamic injection of BB aerosols produces a global clear-sky NET cooling effect at TOA of −0.11 Wm^{-2}, and a clear-sky NET surface cooling effect of −0.38 Wm^{-2}. The temperature gradient from warming the upper troposphere and cooling the surface by dynamic injection compared to surface injection induces compensating wind and climate responses. The climate response from dynamic injection during fire season was very strong over Australia and Congo because of the large temperature gradient in the region accompanied by atmospheric instabilities.

In conclusion, this study has highlighted the significance of integrating wildfire injection height into climate system models to represent more realistically the vertical distribution of BB aerosols and their radiative effects. Utilizing GFDL's AM4.0 model, our research underscores the adequacy of the mechanistic semi-empirical Sofiev injection parametrization for broad-scale aerosol-climate interactions. Moving forward the following uncertainties and developments will be addressed:

- In our calculations of plume height, we apply a uniform daily value for each FRP. Although the influence of diurnal variability of fires on climate may be considered negligible (Veira, Kloster, Wilkenskjeld, & Remy, 2015), the current uniform methodology requires refinement to incorporate the diurnal variability. This is supported by existing research, which highlights the significance of integrating the fire diurnal cycle into estimates of BB emissions (Li et al., 2019). Furthermore, it is important to acknowledge the uncertainties associated with current methods, including the application of a fixed Gaussian distribution to model the fire diurnal cycle, indicating that this area of research remains active within the scientific community (Andela et al., 2015; Li et al., 2019; Zheng et al., 2021).
- The next step in our research involves the implementation of the Sofiev injection methodology within a version of our atmospheric model incorporating comprehensive atmospheric chemistry mechanisms (AM4.1). The significance of applying a full-chemistry model lies in its ability to assess the climatological and air quality impacts resulting from the emission of chemical species by intense BB. Previous studies have already established the critical role of BB emissions in influencing downwind ozone levels and particulate matter concentrations (Palm et al., 2020; Pouyaei et al., 2023; Xu et al., 2021; Ye et al., 2021). By integrating a dynamic injection approach, we aim to enhance the accuracy of simulations regarding the air quality effects of wildfires, thereby offering more realistic insights into their implications under the evolving conditions of our climate.
- We further plan to incorporate interactive estimations of fire emissions and fire smoke injection from our dynamic land component (LM4) within our ESM4 Earth system modeling framework. Such advancements will foster a more comprehensive and interactive approach using information from dynamic fire within LM4 (Rabin et al., 2018), to simulate the atmosphere-vegetation couplings in Earth's climate system and biogeochemical cycles. An interactive land-fire-atmosphere model is required to fully represent the effects from BB aerosols on the climate system, light-absorbing aerosols on snow/ice albedo (Qian et al., 2015), pyrogenic soluble iron on oceanic phytoplankton activates (Ito et al., 2019), and the feedback from these responses on the land. The need for emission-driven climate simulations, which allow for assessing amplification effects of biogeochemical feedbacks (e.g., when climate influences the carbon cycle, producing more climate change, and further influencing carbon cycle), has also been emphasized in the Scenario Model Intercomparison Project (ScenarioMIP) as well as other CMIP6-endorsed MIPs (O'Neill et al., 2016).

Data Availability Statement

The data set used for evaluation of the model was accessed through NASA archives; MODIS AOD (MODIS/Terra Aerosol Cloud Water Vapor Ozone Daily L3 Global 1Deg CMG - LAADS DAAC [Dataset], 2024), AERONET AOD (Aerosol Robotic Network (AERONET) Version 3 AOD Level 2 [Dataset], 2024), CALIPSO extinction profiles (Tackett et al., 2018), MISR plume height project (MISR, 2023). The FRP data set which was used as an input for the model was accessed from FIRMS (Fire Information for Resource Management System - NASA | LANCE | FIRMS [Dataset], 2024), which used fire daily data from MODIS instrument onboard Terra/Aqua satellites (MODIS/Aqua Thermal Anomalies/Fire Daily L3 Global 1km SIN Grid - LAADS DAAC [Dataset], 2024; MODIS/Terra Thermal Anomalies/Fire Daily L3 Global 1km SIN Grid V061 [Dataset], 2024). The global climate model GFDL-AM4.0 which was used in this study is available through GFDL's ftp server (GFDL-AM4 climate model source code, 2024).

Acknowledgments
This study was funded under award NA23OAR4050281I from the National Oceanic and Atmospheric Administration, U.S. Department of Commerce. The statements, findings, conclusions, and recommendations are those of the author(s) and do not necessarily reflect the views of the National Oceanic and Atmospheric Administration, or the U.S. Department of Commerce.

References

Aerosol Robotic Network (AERONET) version 3 AOD level 2 [Dataset]. Retrieved from https://aeronet.gsfc.nasa.gov/new_web/download_all_v3_aod.html

Andela, N., Kaiser, J. W., Van Der Werf, G. R., & Wooster, M. J. (2015). New fire diurnal cycle characterizations to improve fire radiative energy assessments made from MODIS observations. *Atmospheric Chemistry and Physics*, *15*, 8831–8846. https://doi.org/10.5194/ACP-15-8831-2015

Andreae, M. O., Artaxo, P., Fischer, H., Freitas, S. R., Grégoire, J. M., Hansel, A., et al. (2001). Transport of biomass burning smoke to the upper troposphere by deep convection in the equatorial region. *Geophysical Research Letters*, *28*(6), 951–954. https://doi.org/10.1029/2000GL012391

Briggs, G. A. (1984). Plume rise and buoyancy effects. In *Atmospheric science and power production* (Vol. 327, p. 366).

Chimot, J., Veefkind, J. P., Vlemmix, T., & Levelt, P. F. (2018). Spatial distribution analysis of the OMI aerosol layer height: A pixel-by-pixel comparison to CALIOP observations. *Atmospheric Measurement Techniques*, *11*(4), 2257–2277. https://doi.org/10.5194/amt-11-2257-2018

Coogan, S. C. P., Robinne, F.-N., Jain, P., & Flannigan, M. D. (2019). Scientists' warning on wildfire — A Canadian perspective. *Canadian Journal of Forest Research*, *49*(9), 1015–1023. https://doi.org/10.1139/cjfr-2019-0094

Dentener, F., Kinne, S., Bond, T., Boucher, O., Cofala, J., Generoso, S., et al. (2006). Emissions of primary aerosol and precursor gases in the years 2000 and 1750 prescribed data-sets for AeroCom. *Atmospheric Chemistry and Physics*, *6*(12), 4321–4344. https://doi.org/10.5194/ACP-6-4321-2006

Donner, L. J., Wyman, B. L., Hemler, R. S., Horowitz, L. W., Ming, Y., Zhao, M., et al. (2011). The dynamical core, physical parameterizations, and basic simulation characteristics of the atmospheric component AM3 of the GFDL global coupled model CM3. *Journal of Climate*, *24*(13), 3484–3519. https://doi.org/10.1175/2011JCLI3955.1

Dowdy, A. J., & Pepler, A. (2018). Pyroconvection risk in Australia: Climatological changes in atmospheric stability and surface fire weather conditions. *Geophysical Research Letters*, *45*(4), 2005–2013. https://doi.org/10.1002/2017GL076654

Eyring, V., Bony, S., Meehl, G. A., Senior, C. A., Stevens, B., Stouffer, R. J., & Taylor, K. E. (2016). Overview of the Coupled Model Intercomparison Project Phase 6 (CMIP6) experimental design and organization. *Geoscientific Model Development*, *9*(5), 1937–1958. https://doi.org/10.5194/GMD-9-1937-2016

Fasullo, J. T., Rosenbloom, N., & Buchholz, R. (2023). A multiyear tropical Pacific cooling response to recent Australian wildfires in CESM2. *Science Advances*, *9*(19). https://doi.org/10.1126/sciadv.adg1213

Fire information for Resource management system - NASA | LANCE | FIRMS [Dataset]. Retrieved from https://firms.modaps.eosdis.nasa.gov/download/

Flanner, M. G., Zender, C. S., Hess, P. G., Mahowald, N. M., Painter, T. H., Ramanathan, V., & Rasch, P. J. (2009). Springtime warming and reduced snow cover from carbonaceous particles. *Atmospheric Chemistry and Physics*, *9*(7), 2481–2497. https://doi.org/10.5194/ACP-9-2481-2009

Flanner, M. G., Zender, C. S., Randerson, J. T., & Rasch, P. J. (2007). Present-day climate forcing and response from black carbon in snow. *Journal of Geophysical Research*, *112*(D11), 11202. https://doi.org/10.1029/2006JD008003

Ford, B., Val Martin, M., Zelasky, S. E., Fischer, E. V., Anenberg, S. C., Heald, L., & Pierce, J. R. (2018). Future fire impacts on smoke concentrations, visibility, and health in the contiguous United States. *Geohealth*, *2*(8), 229–247. https://doi.org/10.1029/2018gh000144

Freitas, S. R., Longo, K. M., Chatfield, R., Latham, D., Silva Dias, M. A. F., Andreae, M. O., et al. (2007). Including the sub-grid scale plume rise of vegetation fires in low resolution atmospheric transport models. *Atmospheric Chemistry and Physics*, *7*(13), 3385–3398. https://doi.org/10.5194/ACP-7-3385-2007

Freitas, S. R., Longo, K. M., Trentmann, J., & Latham, D. (2010). Technical Note: Sensitivity of 1-D smoke plume rise models to the inclusion of environmental wind drag. *Atmospheric Chemistry and Physics*, *10*(2), 585–594. https://doi.org/10.5194/ACP-10-585-2010

Froyd, K. D., Murphy, D. M., Schill, G. P., & Brock, C. A. (2021). ATom: Measurements from Particle Analysis By Laser Mass Spectrometry (PALMS). https://doi.org/10.3334/ORNLDAAC/1733

Gates, W. L. (1992). AMIP: The atmospheric model intercomparison project. *Bulletin of the American Meteorological Society*, *73*(12), 1962–1970. https://doi.org/10.1175/1520-0477(1992)073<1962:ATAMIP>2.0.CO;2

GFDL-AM4 climate model source code. (2024). Retrieved from https://data1.gfdl.noaa.gov/nomads/forms/am4.0/

Giglio, L., Schroeder, W., & Justice, C. O. (2016). The collection 6 MODIS active fire detection algorithm and fire products. *Remote Sensing of Environment*, *178*, 31–41. https://doi.org/10.1016/J.RSE.2016.02.054

Giles, D. M., Sinyuk, A., Sorokin, M. G., Schafer, J. S., Smirnov, A., Slutsker, I., et al. (2019). Advancements in the Aerosol Robotic Network (AERONET) Version 3 database – automated near-real-time quality control algorithm with improved cloud screening for Sun photometer aerosol optical depth (AOD) measurements. *Atmospheric Measurement Techniques*, *12*(1), 169–209. https://doi.org/10.5194/amt-12-169-2019

Guan, H., Chatfield, R. B., Freitas, S. R., Bergstrom, R. W., & Longo, K. M. (2008). Modeling the effect of plume-rise on the transport of carbon monoxide over Africa with NCAR CAM. *Atmospheric Chemistry and Physics*, *8*(22), 6801–6812. https://doi.org/10.5194/ACP-8-6801-2008

Guo, H., Ming, Y., Fan, S., Wittenberg, A. T., Zhang, R., Zhao, M., & Zhou, L. (2022). Performance of two-moment stratiform microphysics with prognostic precipitation in GFDL's CM4.0. *Journal of Advances in Modeling Earth Systems*, *14*(12), e2022MS003111. https://doi.org/10.1029/2022MS003111

Guo, H., Ming, Y., Fan, S., Zhou, L., Harris, L., & Zhao, M. (2021). Two-moment bulk cloud microphysics with prognostic precipitation in GFDL's atmosphere model AM4.0: Configuration and performance. *Journal of Advances in Modeling Earth Systems*, *13*(6), e2020MS002453. https://doi.org/10.1029/2020MS002453

Harris, L. M., & Lin, S. J. (2013). A two-way nested global-regional dynamical core on the cubed-sphere grid. *Monthly Weather Review*, *141*(1), 283–306. https://doi.org/10.1175/MWR-D-11-00201.1

Held, I. M., Guo, H., Adcroft, A., Dunne, J. P., Horowitz, L. W., Krasting, J., et al. (2019). Structure and performance of GFDL's CM4.0 climate model. *Journal of Advances in Modeling Earth Systems*, *11*, 3691–3727. https://doi.org/10.1029/2019MS001829

Horowitz, L. W., Walters, S., Mauzerall, D. L., Emmons, L. K., Rasch, P. J., Granier, C., et al. (2003). A global simulation of tropospheric ozone and related tracers: Description and evaluation of MOZART, version 2. *Journal of Geophysical Research*, *108*(D24), 4784. https://doi.org/10.1029/2002JD002853

IPCC. (2022). IPCC: Climate change 2022 – Impacts, adaptation and vulnerability, climate change 2022 – Impacts, adaptation and vulnerability. https://doi.org/10.1017/9781009325844

Ito, A., Myriokefalitakis, S., Kanakidou, M., Mahowald, N. M., Scanza, R. A., Hamilton, D. S., et al. (2019). Pyrogenic iron: The missing link to high iron solubility in aerosols. *Science Advances*, *5*. https://doi.org/10.1126/sciadv.aau7671

Jaffe, D. A., & Wigder, N. L. (2012). Ozone production from wildfires: A critical review. *Atmospheric Environment*, *51*, 1–10. https://doi.org/10.1016/J.ATMOSENV.2011.11.063

Jiang, Y., Yang, X. Q., Liu, X., Qian, Y., Zhang, K., Wang, M., et al. (2020). Impacts of wildfire aerosols on global energy budget and climate: The role of climate feedbacks. *Journal of Climate*, *33*(8), 3351–3366. https://doi.org/10.1175/JCLI-D-19-0572.1

Kelly, J. M., Doherty, R. M., O'Connor, F. M., & Mann, G. W. (2018). The impact of biogenic, anthropogenic, and biomass burning volatile organic compound emissions on regional and seasonal variations in secondary organic aerosol. *Atmospheric Chemistry and Physics*, *18*(10), 7393–7422. https://doi.org/10.5194/ACP-18-7393-2018

Koffi, B., Schulz, M., Bréon, F. M., Griesfeller, J., Winker, D., Balkanski, Y., et al. (2012). Application of the CALIOP layer product to evaluate the vertical distribution of aerosols estimated by global models: AeroCom phase I results. *Journal of Geophysical Research*, *117*(D10), 10201. https://doi.org/10.1029/2011JD016858

Lawrence, D. M., Fisher, R. A., Koven, C. D., Oleson, K. W., Swenson, S. C., Bonan, G., et al. (2019). The community land model version 5: Description of new features, benchmarking, and impact of forcing uncertainty. *Journal of Advances in Modeling Earth Systems*, *11*(12), 4245–4287. https://doi.org/10.1029/2018MS001583

Levy, H., Horowitz, L. W., Schwarzkopf, M. D., Ming, Y., Golaz, J. C., Naik, V., & Ramaswamy, V. (2013). The roles of aerosol direct and indirect effects in past and future climate change. *Journal of Geophysical Research: Atmospheres*, *118*(10), 4521–4532. https://doi.org/10.1002/JGRD.50192

Levy, R. C., Mattoo, S., Munchak, L. A., Remer, L. A., Sayer, A. M., Patadia, F., & Hsu, N. C. (2013b). The Collection 6 MODIS aerosol products over land and ocean. *Atmospheric Measurement Techniques*, *6*(11), 2989–3034. https://doi.org/10.5194/AMT-6-2989-2013

Li, F., Ginoux, P., & Ramaswamy, V. (2008). Distribution, transport, and deposition of mineral dust in the Southern Ocean and Antarctica: Contribution of major sources. *Journal of Geophysical Research*, *113*(D10). https://doi.org/10.1029/2007JD009190

Li, F., Zhang, X., Roy, D. P., & Kondragunta, S. (2019). Estimation of biomass-burning emissions by fusing the fire radiative power retrievals from polar-orbiting and geostationary satellites across the conterminous United States. *Atmospheric Environment*, *211*, 274–287. https://doi.org/10.1016/J.ATMOSENV.2019.05.017

Li, J., Carlson, B. E., Yung, Y. L., Lv, D., Hansen, J., Penner, J. E., et al. (2022). Scattering and absorbing aerosols in the climate system. *Nature Reviews Earth & Environment*, *3*(6), 363–379. https://doi.org/10.1038/s43017-022-00296-7

Li, Y., Tong, D., Ma, S., Freitas, S. R., Ahmadov, R., Sofiev, M., et al. (2023). Impacts of estimated plume rise on PM2.5 exceedance prediction during extreme wildfire events: A comparison of three schemes (Briggs, Freitas, and Sofiev). *Atmospheric Chemistry and Physics*, *23*(5), 3083–3101. https://doi.org/10.5194/ACP-23-3083-2023

Liu, D., Hu, K., Zhao, D., Ding, S., Wu, Y., Zhou, C., et al. (2020). Efficient vertical transport of black carbon in the planetary boundary layer. *Geophysical Research Letters*, *47*(15), e2020GL088858. https://doi.org/10.1029/2020GL088858

Liu, M., Lin, J., Boersma, K. F., Pinardi, G., Wang, Y., Chimot, J., et al. (2019). Improved aerosol correction for OMI tropospheric NO_2 retrieval over East Asia: Constraint from CALIOP aerosol vertical profile. *Atmospheric Measurement Techniques*, *12*(1), 1–21. https://doi.org/10.5194/amt-12-1-2019

Lu, Z., Liu, X., Ke, Z., Zhang, K., Ma, P. L., & Fan, J. (2024). Incorporating an interactive fire plume-rise model in the DOE's energy Exascale Earth System Model version 1 (E3SMv1) and examining aerosol radiative effect. *Journal of Advances in Modeling Earth Systems*, *16*, e2023MS003818. https://doi.org/10.1029/2023MS003818

Ma, C., Ni, R., Su, H., & Cheng, Y. (2024). Enhancing global simulation of smoke injection height for intense pyro-convection through coupling an improved one-dimensional plume rise model in CAM-chem. *Journal of Advances in Modeling Earth Systems*, *16*(10), e2023MS004127. https://doi.org/10.1029/2023MS004127

Mahowald, N. M., Scanza, R., Brahney, J., Goodale, C. L., Hess, P. G., Moore, J. K., & Neff, J. (2017). Aerosol deposition impacts on land and ocean carbon cycles. *Current Climate Change Reports*, *3*(1), 16–31. https://doi.org/10.1007/S40641-017-0056-Z/FIGURES/3

Malavelle, F. F., Haywood, J. M., Mercado, L. M., Folberth, G. A., Bellouin, N., Sitch, S., & Artaxo, P. (2019). Studying the impact of biomass burning aerosol radiative and climate effects on the Amazon rainforest productivity with an Earth system model. *Atmospheric Chemistry and Physics*, *19*(2), 1301–1326. https://doi.org/10.5194/ACP-19-1301-2019

Martin, M. V., Kahn, R. A., & Tosca, M. G. (2018). A global analysis of wildfire smoke injection heights derived from space-based multi-angle imaging. *Remote Sensing*, *10*, 1609. https://doi.org/10.3390/RS10101609

Meinshausen, M., Vogel, E., Nauels, A., Lorbacher, K., Meinshausen, N., Etheridge, D. M., et al. (2017). Historical greenhouse gas concentrations for climate modelling (CMIP6). *Geoscientific Model Development*, *10*(5), 2057–2116. https://doi.org/10.5194/gmd-10-2057-2017

Menut, L., Bessagnet, B., Briant, R., Cholakian, A., Couvidat, F., Mailler, S., et al. (2021). The CHIMERE v2020r1 online chemistry-transport model. *Geoscientific Model Development*, *14*(11), 6781–6811. https://doi.org/10.5194/GMD-14-6781-2021

Menut, L., Flamant, C., Turquety, S., Deroubaix, A., Chazette, P., & Meynadier, R. (2018). Impact of biomass burning on pollutant surface concentrations in megacities of the Gulf of Guinea. *Atmospheric Chemistry and Physics*, *18*(4), 2687–2707. https://doi.org/10.5194/ACP-18-2687-2018

MISR. Retrieved from https://misr.jpl.nasa.gov/get-data/misr-plume-height-project-2/

MODIS/Aqua Thermal Anomalies/Fire Daily L3 Global 1km SIN Grid [Dataset]. Retrieved from https://ladsweb.modaps.eosdis.nasa.gov/missions-and-measurements/products/MYD14A1

MODIS/Terra Aerosol Cloud Water Vapor Ozone Daily L3 Global 1Deg CMG [Dataset]. Retrieved from https://ladsweb.modaps.eosdis.nasa.gov/missions-and-measurements/products/MOD08_D3

MODIS/Terra Thermal Anomalies/Fire Daily L3 Global 1km SIN Grid [Dataset]. Retrieved from https://ladsweb.modaps.eosdis.nasa.gov/missions-and-measurements/products/MOD14A1

Naik, V., Horowitz, L. W., Fiore, A. M., Ginoux, P., Mao, J., Aghedo, A. M., & Levy, H. (2013). Impact of preindustrial to present-day changes in short-lived pollutant emissions on atmospheric composition and climate forcing. *Journal of Geophysical Research: Atmospheres*, *118*(14), 8086–8110. https://doi.org/10.1002/JGRD.50608

Nanda, S., de Graaf, M., Veefkind, J. P., Sneep, M., ter Linden, M., Sun, J., & Levelt, P. F. (2020). A first comparison of TROPOMI aerosol layer height (ALH) to CALIOP data. *Atmospheric Measurement Techniques*, *13*(6), 3043–3059. https://doi.org/10.5194/amt-13-3043-2020

NCEP/NCAR global reanalysis products, 1948-continuing [Dataset]. Retrieved from https://rda.ucar.edu/datasets/d090000/

O'Dowd, C. D., Langmann, B., Varghese, S., Scannell, C., Ceburnis, D., & Facchini, M. C. (2008). A combined organic-inorganic sea-spray source function. *Geophysical Research Letters*, *35*(1). https://doi.org/10.1029/2007GL030331

Ohneiser, K., Ansmann, A., Witthuhn, J., Deneke, H., Chudnovsky, A., Walter, G., & Senf, F. (2023). Self-lofting of wildfire smoke in the troposphere and stratosphere: Simulations and space lidar observations. *Atmospheric Chemistry and Physics*, *23*(4), 2901–2925. https://doi.org/10.5194/ACP-23-2901-2023

O'Neill, B. C., Tebaldi, C., Van Vuuren, D. P., Eyring, V., Friedlingstein, P., Hurtt, G., et al. (2016). The Scenario Model Intercomparison Project (ScenarioMIP) for CMIP6. *Geoscientific Model Development*, *9*, 3461–3482. https://doi.org/10.5194/GMD-9-3461-2016

Palm, B. B., Peng, Q., Fredrickson, C. D., Lee, B. H., Garofalo, L. A., Pothier, M. A., et al. (2020). Quantification of organic aerosol and brown carbon evolution in fresh wildfire plumes. *Proceedings of the National Academy of Sciences*, *117*(47), 29469–29477. https://doi.org/10.1073/pnas.2012218117

Pan, X., Ichoku, C., Chin, M., Bian, H., Darmenov, A., Colarco, P., et al. (2020). Six global biomass burning emission datasets: Intercomparison and application in one global aerosol model. *Atmospheric Chemistry and Physics*, *20*(2), 969–994. https://doi.org/10.5194/ACP-20-969-2020

Paugam, R., Wooster, M., Freitas, S., & Val Martin, M. (2016). A review of approaches to estimate wildfire plume injection height within large-scale atmospheric chemical transport models. *Atmospheric Chemistry and Physics*, *16*(2), 907–925. https://doi.org/10.5194/ACP-16-907-2016

Permadi, D. A., Oanh, N. T. K., & Vautard, R. (2018). Integrated emission inventory and modeling to assess distribution of particulate matter mass and black carbon composition in Southeast Asia. *Atmospheric Chemistry and Physics*, *18*(4), 2725–2747. https://doi.org/10.5194/ACP-18-2725-2018

Peterson, D., Hyer, E., & Wang, J. (2014). Quantifying the potential for high-altitude smoke injection in the North American boreal forest using the standard MODIS fire products and subpixel-based methods. *Journal of Geophysical Research: Atmospheres*, *119*(6), 3401–3419. https://doi.org/10.1002/2013JD021067

Peterson, D., Wang, J., Ichoku, C., Hyer, E., & Ambrosia, V. (2013). A sub-pixel-based calculation of fire radiative power from MODIS observations: 1: Algorithm development and initial assessment. *Remote Sensing of Environment*, *129*, 262–279. https://doi.org/10.1016/J.RSE.2012.10.036

Pouyaei, A., Mizzi, A. P., Choi, Y., Mousavinezhad, S., & Khorshidian, N. (2023). Downwind ozone changes of the 2019 Williams flats wildfire: Insights from WRF-chem/DART assimilation of OMI NO2, HCHO, and MODIS AOD retrievals. *Journal of Geophysical Research: Atmospheres*, *128*(11), e2022JD038019. https://doi.org/10.1029/2022JD038019

Pouyaei, A., Sadeghi, B., Choi, Y., Jung, J., Souri, A. H., Zhao, C., & Song, C. H. (2021). Development and implementation of a physics-based convective mixing scheme in the community multiscale air quality modeling framework. *Journal of Advances in Modeling Earth Systems*, *13*(6), e2021MS002475. https://doi.org/10.1029/2021MS002475

Qian, Y., Yasunari, T. J., Doherty, S. J., Flanner, M. G., Lau, W. K. M., Ming, J., et al. (2015). Light-absorbing particles in snow and ice: Measurement and modeling of climatic and hydrological impact. *Advances in Atmospheric Sciences*, *32*(1), 64–91. https://doi.org/10.1007/S00376-014-0010-0/METRICS

Rabin, S. S., Melton, J. R., Lasslop, G., Bachelet, D., Forrest, M., Hantson, S., et al. (2017). The Fire Modeling Intercomparison Project (FireMIP), phase 1: Experimental and analytical protocols with detailed model descriptions. *Geoscientific Model Development*, *10*(3), 1175–1197. https://doi.org/10.5194/GMD-10-1175-2017

Rabin, S. S., Ward, D. S., Malyshev, S. L., Magi, B. I., Shevliakova, E., & Pacala, S. W. (2018). A fire model with distinct crop, pasture, and non-agricultural burning: Use of new data and a model-fitting algorithm for FINAL.1. *Geoscientific Model Development*, *11*(2), 815–842. https://doi.org/10.5194/GMD-11-815-2018

Raffuse, S. M., Craig, K. J., Larkin, N. K., Strand, T. T., Sullivan, D. C., Wheeler, N. J. M., & Solomon, R. (2012). An evaluation of modeled plume injection height with satellite-derived observed plume height. *Atmosphere*, *3*(1), 103–123. https://doi.org/10.3390/ATMOS3010103

Ramanathan, V., Callis, L., Cess, R., Hansen, J., Isaksen, I., Kuhn, W., et al. (1987). Climate-chemical interactions and effects of changing atmospheric trace gases. *Reviews of Geophysics*, *25*(7), 1441–1482. https://doi.org/10.1029/RG025I007P01441

Randerson, J. T., Van der Werf, G. R., Giglio, L., Collatz, G. J., & Kasibhatla, P. S. (2015). *Global fire emissions database, version 4.1 (GFEDv4)*. ORNL DAAC. https://doi.org/10.3334/ORNLDAAC/1293

Randles, C. A., & Ramaswamy, V. (2010). Direct and semi-direct impacts of absorbing biomass burning aerosol on the climate of southern Africa: A Geophysical Fluid Dynamics Laboratory GCM sensitivity study. *Atmospheric Chemistry and Physics*, *10*(20), 9819–9831. https://doi.org/10.5194/ACP-10-9819-2010

Rémy, S., Veira, A., Paugam, R., Sofiev, M., Kaiser, J. W., Marenco, F., et al. (2017). Two global data sets of daily fire emission injection heights since 2003. *Atmospheric Chemistry and Physics*, *17*(4), 2921–2942. https://doi.org/10.5194/ACP-17-2921-2017

Rio, C., Hourdin, F., & Chãdin, A. (2010). Numerical simulation of tropospheric injection of biomass burning products by pyro-thermal plumes. *Atmospheric Chemistry and Physics*, *10*(8), 3463–3478. https://doi.org/10.5194/ACP-10-3463-2010

Sayer, A. M., Munchak, L. A., Hsu, N. C., Levy, R. C., Bettenhausen, C., & Jeong, M. J. (2014). MODIS Collection 6 aerosol products: Comparison between Aqua's e-Deep Blue, Dark Target, and "merged" data sets, and usage recommendations. *Journal of Geophysical Research: Atmospheres*, *119*(24), 13965–13989. https://doi.org/10.1002/2014JD022453

Sinyuk, A., Sinyuk, A., Holben, B. N., Eck, T. F., Eck, T. F., M. Giles, D., et al. (2020). The AERONET Version 3 aerosol retrieval algorithm, associated uncertainties and comparisons to Version 2. *Atmospheric Measurement Techniques*, *13*(6), 3375–3411. https://doi.org/10.5194/AMT-13-3375-2020

Sofiev, M., Ermakova, T., & Vankevich, R. (2012). Evaluation of the smoke-injection height from wild-land fires using remote-sensing data. *Atmospheric Chemistry and Physics*, *12*(4), 1995–2006. https://doi.org/10.5194/ACP-12-1995-2012

Tackett, J. L., Winker, D. M., Getzewich, B. J., Vaughan, M. A., Young, S. A., & Kar, J. (2018). CALIPSO lidar level 3 aerosol profile product: Version 3 algorithm design. *Atmospheric Measurement Techniques*, *11*(7), 4129–4152. https://doi.org/10.5194/AMT-11-4129-2018

Taylor, K. E., Williamson, D., & Zwiers, F. (2000). *The sea surface temperature and sea-ice concentration boundary conditions for AMIP II simulations*. Retrieved from https://pcmdi.llnl.gov/report/pdf/60.pdf

Thapa, L. H., Ye, X., Hair, J. W., Fenn, M. A., Shingler, T., Kondragunta, S., et al. (2022). Heat flux assumptions contribute to overestimation of wildfire smoke injection into the free troposphere. *Communications Earth & Environment*, *3*(1), 1–11. https://doi.org/10.1038/s43247-022-00563-x

Thorsen, T. J., Ferrare, R. A., Kato, S., & Winker, D. M. (2020). Aerosol direct radiative effect sensitivity analysis. *Journal of Climate*, *33*(14), 6119–6139. https://doi.org/10.1175/JCLI-D-19-0669.1

Tosca, M. G., Randerson, J. T., & Zender, C. S. (2013). Global impact of smoke aerosols from landscape fires on climate and the Hadley circulation. *Atmospheric Chemistry and Physics*, *13*(10), 5227–5241. https://doi.org/10.5194/ACP-13-5227-2013

Val Martin, M., Kahn, R. A., Logan, J. A., Paugam, R., Wooster, M., & Ichoku, C. (2012). Space-based observational constraints for 1-D fire smoke plume-rise models. *Journal of Geophysical Research*, *117*(D22), 22204. https://doi.org/10.1029/2012JD018370

Val Martin, M., Logan, J. A., Kahn, R. A., Leung, F. Y., Nelson, D. L., & Diner, D. J. (2010). Smoke injection heights from fires in North America: Analysis of 5 years of satellite observations. *Atmospheric Chemistry and Physics*, *10*(4), 1491–1510. https://doi.org/10.5194/ACP-10-1491-2010

Veira, A., Kloster, S., Schutgens, N. A. J., & Kaiser, J. W. (2015). Fire emission heights in the climate system – Part 2: Impact on transport, black carbon concentrations and radiation. *Atmospheric Chemistry and Physics*, *15*(13), 7173–7193. https://doi.org/10.5194/acp-15-7173-2015

Veira, A., Kloster, S., Wilkenskjeld, S., & Remy, S. (2015). Fire emission heights in the climate system – Part 1: Global plume height patterns simulated by ECHAM6-HAM2. *Atmospheric Chemistry and Physics*, *15*(13), 7155–7171. https://doi.org/10.5194/acp-15-7155-2015

Ward, D. S., Shevliakova, E., Malyshev, S., & Rabin, S. (2018). Trends and variability of global fire emissions due to historical anthropogenic activities. *Global Biogeochemical Cycles*, *32*(1), 122–142. https://doi.org/10.1002/2017GB005787

Westerling, A. L., Hidalgo, H. G., Cayan, D. R., & Swetnam, T. W. (2006). Warming and earlier spring increase western U.S. forest wildfire activity. *Science*, *313*(5789), 940–943. https://doi.org/10.1126/science.1128834

Xie, Y., Lin, M., Decharme, B., Delire, C., Horowitz, L. W., Lawrence, D. M., et al. (2022). Tripling of western US particulate pollution from wildfires in a warming climate. *Proceedings of the National Academy of Sciences*, *119*(14), e2111372119. https://doi.org/10.1073/pnas.2111372119

Xu, L., Crounse, J. D., Vasquez, K. T., Allen, H., Wennberg, P. O., Bourgeois, I., et al. (2021). Ozone chemistry in western U.S. wildfire plumes. *Science Advances*, *7*(50), 3648. https://doi.org/10.1126/sciadv.abl3648

Yasunari, T. J., Nakamura, H., Kim, K. M., Choi, N., Lee, M. I., Tachibana, Y., & Da Silva, A. M. (2021). Relationship between circum-Arctic atmospheric wave patterns and large-scale wildfires in boreal summer. *Environmental Research Letters*, *16*(6), 064009. https://doi.org/10.1088/1748-9326/ABF7EF

Ye, X., Arab, P., Ahmadov, R., James, E., Grell, G. A., Pierce, B., et al. (2021). Evaluation and intercomparison of wildfire smoke forecasts from multiple modeling systems for the 2019 Williams Flats fire. *Atmospheric Chemistry and Physics*, *21*(18), 14427–14469. https://doi.org/10.5194/ACP-21-14427-2021

Yu, Y., Dunne, J. P., Shevliakova, E., Ginoux, P., Malyshev, S., John, J. G., & Krasting, J. P. (2021). Increased risk of the 2019 Alaskan July fires due to anthropogenic activity. *Bulletin of the American Meteorological Society*, *102*(1), S1–S7. https://doi.org/10.1175/BAMS-D-20-0154.1

Yu, Y., & Ginoux, P. (2021). Assessing the contribution of the ENSO and MJO to Australian dust activity based on satellite- and ground-based observations. *Atmospheric Chemistry and Physics*, *21*(11), 8511–8530. https://doi.org/10.5194/ACP-21-8511-2021

Zhao, M., Golaz, J. C., Held, I. M., Guo, H., Balaji, V., Benson, R., et al. (2018a). The GFDL global atmosphere and land model AM4.0/LM4.0: 1. Simulation characteristics with prescribed SSTs. *Journal of Advances in Modeling Earth Systems*, *10*(3), 691–734. https://doi.org/10.1002/2017MS001208

Zhao, M., Golaz, J. C., Held, I. M., Guo, H., Balaji, V., Benson, R., et al. (2018b). The GFDL global atmosphere and land model AM4.0/LM4.0: 2. Model description, sensitivity studies, and tuning strategies. *Journal of Advances in Modeling Earth Systems*, *10*(3), 735–769. https://doi.org/10.1002/2017MS001209

Zhao, M., Held, I. M., Lin, S. J., & Vecchi, G. A. (2009). Simulations of global Hurricane climatology, interannual variability, and response to global warming using a 50-km resolution GCM. *Journal of Climate*, *22*(24), 6653–6678. https://doi.org/10.1175/2009JCLI3049.1

Zheng, Y., Liu, J., Jian, H., Fan, X., & Yan, F. (2021). Fire diurnal cycle derived from a combination of the Himawari-8 and VIIRS satellites to improve fire emission assessments in Southeast Australia. *Remote Sensing*, *13*(15), 2852. https://doi.org/10.3390/RS13152852

Zhu, L., Val Martin, M., Gatti, L. V., Kahn, R., Hecobian, A., & Fischer, E. V. (2018). Development and implementation of a new biomass burning emissions injection height scheme (BBEIH v1.0) for the GEOS-Chem model (v9-01-01). *Geoscientific Model Development*, *11*(10), 4103–4116. https://doi.org/10.5194/GMD-11-4103-2018